NAVAL POSTGRADUATE SCHOOL

MONTEREY, CALIFORNIA

THESIS

ADDITION OF A SECOND ATOMIC SOURCE FOR A DUAL BEAM ATOM SENSOR

by

Darryl Gervis

September 2021

Thesis Advisor: Francesco A. Narducci
Second Reader: Jeffrey G. Lee

THIS PAGE INTENTIONALLY LEFT BLANK

REPORT DOCUMENTATION PAGE			Form Approved OMB No. 0704-0188

1. AGENCY USE ONLY *(Leave blank)*	2. REPORT DATE September 2021	3. REPORT TYPE AND DATES COVERED Master's thesis

4. TITLE AND SUBTITLE ADDITION OF A SECOND ATOMIC SOURCE FOR A DUAL BEAM ATOM SENSOR	5. FUNDING NUMBERS RPP86
6. AUTHOR(S) Darryl Gervis	
7. PERFORMING ORGANIZATION NAME(S) AND ADDRESS(ES) Naval Postgraduate School Monterey, CA 93943-5000	8. PERFORMING ORGANIZATION REPORT NUMBER
9. SPONSORING / MONITORING AGENCY NAME(S) AND ADDRESS(ES) PEO IWS	10. SPONSORING / MONITORING AGENCY REPORT NUMBER

11. SUPPLEMENTARY NOTES The views expressed in this thesis are those of the author and do not reflect the official policy or position of the Department of Defense or the U.S. Government.

12a. DISTRIBUTION / AVAILABILITY STATEMENT Approved for public release. Distribution is unlimited.	12b. DISTRIBUTION CODE A

13. ABSTRACT (maximum 200 words)

Ring laser gyroscope (RLG)-based inertial navigation systems (INS) form the basis of navigation systems. While RLG-based systems have an improvement in accuracy and reliability over their traditional mechanical gyroscope-based forebearers, they suffer inaccuracies and drift in detecting acceleration and rotation that lead to errors. INS compute their current position by integrating equations of motion from their last position, and therefore any error can quickly compound. Atomic beam gyroscopes offer a major advantage over current ring laser-based systems in that they can have a potential increased accuracy of several orders of magnitude, which results in far more accurate navigation over time while in operation. By linking gyroscope parameters to atomic parameters (which, by definition, do not change over time), atomic gyroscopes have low drift. The test bed at Naval Postgraduate School uses one atomic beam that can detect but cannot distinguish between rotation and acceleration. This research involves the addition of a second anti-parallel beam path to the apparatus with enhanced optical characteristics and changes to the detection and state lasers to allow the apparatus to distinguish between the two forms of motion. The velocity, divergence, and optimal power settings of the second atomic beam are characterized, and the changes to the detection and state lasers to allow for simultaneous bi-directional measurement are discussed.

14. SUBJECT TERMS quantum, gyroscope, accelerometer, atom beam, inertial navigation, laser, FORCEnet, atom interferometry, Raman	15. NUMBER OF PAGES 83
	16. PRICE CODE

17. SECURITY CLASSIFICATION OF REPORT	18. SECURITY CLASSIFICATION OF THIS PAGE	19. SECURITY CLASSIFICATION OF ABSTRACT	20. LIMITATION OF ABSTRACT
Unclassified	Unclassified	Unclassified	UU

NSN 7540-01-280-5500

Standard Form 298 (Rev. 2-89)
Prescribed by ANSI Std. 239-18

THIS PAGE INTENTIONALLY LEFT BLANK

Approved for public release. Distribution is unlimited.

ADDITION OF A SECOND ATOMIC SOURCE FOR A DUAL BEAM ATOM SENSOR

Darryl Gervis
Lieutenant Commander, Royal Canadian Navy
BCE, Royal Military College of Canada, 2003

Submitted in partial fulfillment of the
requirements for the degree of

MASTER OF SCIENCE IN APPLIED PHYSICS

from the

NAVAL POSTGRADUATE SCHOOL
September 2021

Approved by: Francesco A. Narducci
Advisor

Jeffrey G. Lee
Second Reader

Joseph P. Hooper
Chair, Department of Physics

THIS PAGE INTENTIONALLY LEFT BLANK

ABSTRACT

Ring laser gyroscope (RLG)-based inertial navigation systems (INS) form the basis of navigation systems. While RLG-based systems have an improvement in accuracy and reliability over their traditional mechanical gyroscope-based forebearers, they suffer inaccuracies and drift in detecting acceleration and rotation that lead to errors. INS compute their current position by integrating equations of motion from their last position, and therefore any error can quickly compound. Atomic beam gyroscopes offer a major advantage over current ring laser-based systems in that they can have a potential increased accuracy of several orders of magnitude, which results in far more accurate navigation over time while in operation. By linking gyroscope parameters to atomic parameters (which, by definition, do not change over time), atomic gyroscopes have low drift. The test bed at Naval Postgraduate School uses one atomic beam that can detect but cannot distinguish between rotation and acceleration. This research involves the addition of a second anti-parallel beam path to the apparatus with enhanced optical characteristics and changes to the detection and state lasers to allow the apparatus to distinguish between the two forms of motion. The velocity, divergence, and optimal power settings of the second atomic beam are characterized, and the changes to the detection and state lasers to allow for simultaneous bi-directional measurement are discussed.

THIS PAGE INTENTIONALLY LEFT BLANK

Table of Contents

List of Figures

THIS PAGE INTENTIONALLY LEFT BLANK

List of Tables

THIS PAGE INTENTIONALLY LEFT BLANK

List of Acronyms and Abbreviations

2D-MOT	two-dimensional magneto-optical trap
AOM	acousto-optic modulator
FWHM	full width at half maximum
HWP	half-wave plate
GPS	Global Positioning System
INS	inertial navigation systems
PBS	polarizing beam splitter
MOT	magneto optical trap
PMT	photomultiplier tube
QWP	quarter-wave plate
RLG	ring laser gyro
SAB	signal above background
SATABS	saturated absorption spectrum
SNR	signal-to-noise ratio

THIS PAGE INTENTIONALLY LEFT BLANK

Executive Summary

Atomic gyroscopes represent a generational leap in inertial measurement unit design. Building on the ring laser gyro based systems that came before, atomic gyros can provide an ultra low drift solution to inertial measurement. By taking advantage of atomic properties the drift rate has the potential to be much lower than currently field RLG units. This allows for extended navigation in areas where the Global positioning system is actively denied or simply unavailable (for instance a submarine operating submerged).

Although atomic gyroscope technologies are still in their relative infancy, NPS has constructed a quantum gyroscope apparatus that has a single unidirectional atomic beam. This includes a single functioning two-dimensional magneto optical trap (2D-MOT). This paper will build on the work previously done within the Quantum Group and augment the current apparatus with the addition of a second anti-parallel beam. This addition will allow the apparatus to measure and distinguish between rotation and acceleration. The beam addition will require the construction of an entirely new cage assembly for the creation of a second 2D-MOT. Several new design elements will be incorporated into the cage design, allowing for increased functionality and more efficient MOT design, leading to a stronger atomic beam and higher signal levels. Key challenges in bi-direction detection will also be examined and discussed.

Atomic beam gyroscopes show great promise and can fundamentally change the way we navigate. By reducing or even functionally eliminating the need for GPS, atomic beam based INS systems offer a an interesting way forward for military navigation and, by extension, many uses in the civilian world as well. In much the same way that GPS wrought systemic changes in the United States military in the middle of the 20th century, quantum INS technologies have the potential to fundamentally change the way we navigate.

THIS PAGE INTENTIONALLY LEFT BLANK

Acknowledgments

I would like to thank the faculty and staff at the Naval Postgraduate School for their fantastic instruction and unwavering support. First and foremost in my thanks is Dr. Frank Narducci, my ever-patient thesis advisor. I am eternally grateful for his keen guidance and expert knowledge, and for the technical support he provided over the last year. In addition, I'd like to thank Dr. Jeffery Lee for his outstanding assistance in the lab, be it in constructing the new cage assembly or dealing with my many, many questions. To my good friends in the Scythe crew, thank you for your camaraderie and for making this foreigner feel at home over the past two years. Last but certainly not least is my amazing wife, Jennifer Bond. Without her love and support over the last two years, none of this would have been possible.

THIS PAGE INTENTIONALLY LEFT BLANK

CHAPTER 1:
Introduction

In this chapter, I will review the background information motivating reasons for developing an atomic gyroscope, and lay out the challenges in the development of this technology. Starting with the development of the Global Positioning System (GPS) in the 1980s, through competing technological advancements in inertial navigation systems from the 1960s, to our current ring laser gyro systems (RLG), I will cover the advantages and disadvantages of our current systems and why the atomic gyroscope is such an exciting and promising future sensor.

1.1 Global Position System

First started as a Department of Defense Project in the 1970s, the Global Positioning System (GPS) is a constellation of 31 satellites in Earth's orbit that transmit navigational information with global coverage. On a basic and fundamental level, the system operates by each satellite knowing its own position to a high degree of accuracy, as well as having access to highly accurate atomic clocks. By transmitting their location and a timestamp to a handheld or vehicle mounted receiver, the receiver is able to triangulate its position with an accuracy of a few meters to a few centimetres, depending on coverage and number of satellites received [1].

Opened to civilian use in the 1980s, GPS accuracy for civilian users was initially deliberately reduced. Since the year 2000, however, full accuracy has been made available to all, leading to a significant number of uses and users across all facets of industry and society. While GPS was the first system available, since its launch, several countries have initiated their own similar constellations, including Russian's GLONASS, China's BeiDou, and the European Union's Galileo positioning system [2]. Each has its own unique features, but all operate using the same principles.

The mass adoption of these systems and their ease of use, combined with high accuracy, revolutionized warfare. Suddenly, aircraft, ships, tanks, and even soldiers in the field could have real time, extremely low error positional information. This capability allowed for a measure of precision and planning in warfare that had not previously been possible. From strike missiles being launched from a submarine with an accurately known position underwater, to using GPS to conduct counter-battery artillery fire, over the past four decades, this technology has revolutionized military capability and planning. Additionally, GPS technology has become so ubiquitous in daily civilian life—for example in cellular phones, and passenger vehicles—that it is hardly given much thought.

However, in a military environment, GPS is not infallible. Due to the low power and distance to the satellites, GPS signals are weak and can be easily jammed with relatively common equipment such as a simple microwave oven. Recent conflicts, such as the insurgency in Ukraine and conflicts in the Middle East have shown that relying on GPS as one's sole method of navigation could have disastrous consequences when against a technologically adept adversary with GPS denial capability [3].

It was these drawbacks that saw an increased interest in developing and improving existing navigation technologies in the 2000s that would work with, and more importantly, work independently from, GPS should the system fail or be jammed during a future conflict.

1.2 Inertial Navigation Systems

Inertial navigation systems (INS) are the solution to the systemic issues with GPS. Unlike GPS, they do not require an outside signal to work, as they are a black box solution—once they are fed with an initial position, they compute the position using a navigation technique known as dead reckoning. By starting with a known position and measuring a platforms rotation and acceleration, the system can infer a later position without the need for a GPS signal. The system does not require an external signal so there is nothing to jam or disrupt.

1.2.1 Mechanical Gyroscopes

Inertial navigation systems are not new. Developed for missiles during World War II, their use was widespread prior to the roll-out of GPS among ships and submarines that required a relatively accurate position whilst away from land, where there were no landmarks from which to navigate. These early systems were based on mechanical gyroscopes. They were large, heavy, and prone to mechanical failure. They were also very susceptible to navigational error—known as drift—and the longer they operated the more the error compounded.

These first INS systems took advantage of the properties of mechanical gyroscopes to provide a reference for rotation, as a gyroscope that is spun up will try and remain pointed in the same direction while spinning. Combined with measurement units for linear acceleration, these INS systems had all the necessary sensors to accurately determine motion over time and could be made exceedingly accurate. That said, the mechanical gyroscopes used in the first INS systems had a huge drawback: friction [5]. This friction caused a significant source of drift and wear on the equipment, and would eventually lead to mechanical failure. These drawbacks were known early

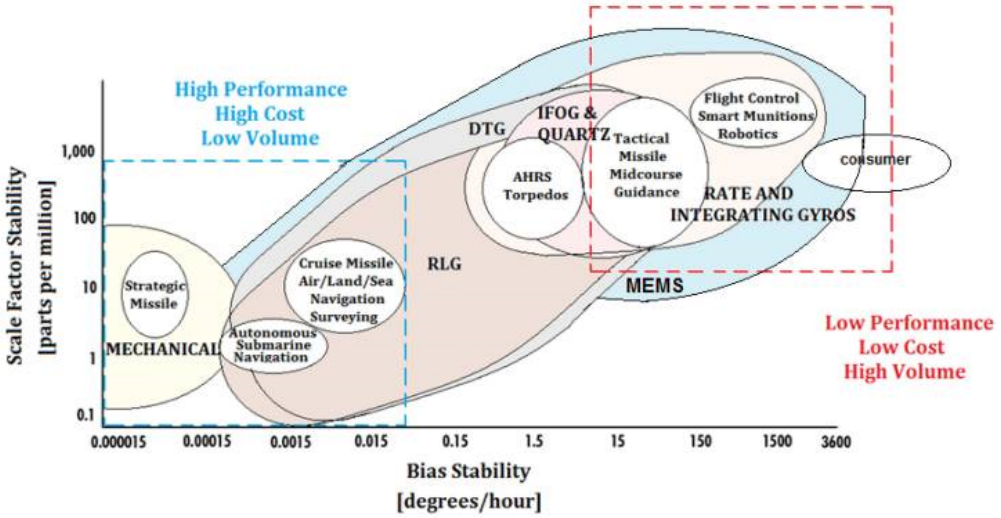

Figure 1.1. A diagram of some commonly used INS systems, grouped cost/-complexity on the vertical axis and accuracy over time on the horizontal. Source: [4]

on, and throughout the mid-20th century there were many attempts at building a better system. This eventually led to the development of ring laser gyroscope-based systems.

1.2.2 Ring Laser Gyroscopes

The Ring laser gyroscope (RLG) was developed to improve on many of the shortcomings of the earlier mechanical systems. In an RLG, mechanical gyroscopes are replaced by an optical setup where one beam of light is split into two beams that then travel the same path but in opposite directions. At the end of their path, the beams are split off into a specialized detector that measures the fringing of the interference between the two. If the system is under rotation, light following one path will "chase the mirrors" thereby traveling farther than light traveling along the other path. The change in path lengths causes a shift in the phase of the fringe pattern which can be correlated back to the rotation rate. If the system is not rotating, then no phase shift in the interference path will be observed. This is known as the Sagnac effect, and is the fundamental theory behind RLG operation.

Ring laser gyroscopes were first deployed in the late 1980s and saw widespread adoption in armed forces and civilian industries (such as commercial airliners) around the world by the turn of the century. They boast several advantages over their mechanical forebears. Few moving parts means no friction, which cuts down a significant source of drift. It also means lower power requirements, reduced size footprint, and far less maintenance required [4].

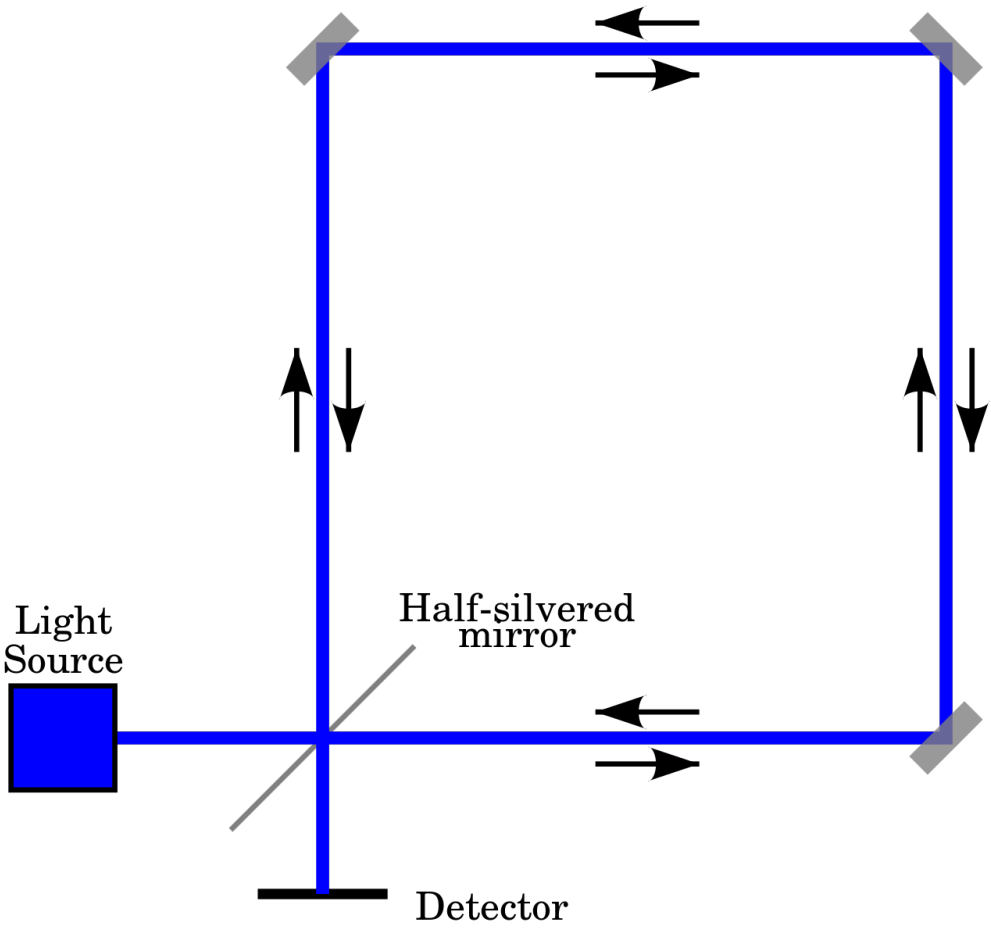

Figure 1.2. A typical RLG Setup using the Sagnac effect. Source: [6].

Based on the above discussion, one can ask about the need for atomic gyroscopes? Despite all the advantages, a modern RLG based INS can still drift up to one nautical mile every 24 hours under normal use and still be considered within specification [7]. Additionally, they require some moving parts, specifically, a dithering motor in order to help resist frequency locking—a form of error to which RLG's are prone in low rotation rate environments. In a frequency locking condition, the two frequencies of the counter rotating beams become almost identical and locked together. This locking leads to the standing wave getting locked to one frequency, and thus rotation will not be observed as the fringing pattern will not be altered. As with mechanical systems, errors in RLG measurement of rotation rate are compounded the longer the system is run without GPS input to "reset" the error, and can be particularly significant in submarines operating without GPS for weeks at a time.

However, RLG-based systems have seen significant upgrades since the late 1980s. Several nations

are now fielding a new subset of RLG-based systems using fiber optics, which eliminates the need for dithering and thus creates a true solid state sensor [8]. Even with these new developments, RLG are all fundamentally limited by the property of their particle of measure - in this case, the photon. The effective mass of the photon is one of the fundamental limits of RLG sensitivity. Thus, there exists a requirement to move into the next phase in navigation system design that shows massive potential for a true generational leap in reducing drift while still retaining all the advantages of the RLG system that preceded them. Atomic gyroscopes are a promising technology that can satisfy this requirement.

1.3 Atomic Gyroscopes

Atomic gyroscopes were first developed in the early 1990s. Following the first published papers in 1991 [9], [10], [11] and 1992 [12], there has been a large interest in this developing field due to the inherent sensitivity benefits of using atoms. Atomic interferometry has since been used for determining the fine constant [13] and measuring gravity [14]. In 2006, the first uses of atomic interferometry in inertial measurement took place [15], [16], [17], [18], showing the advantages in overall sensitivity when using atoms instead of photons.

The fundamental difference between an atomic gyroscope and an optical gyroscope is that instead of a beam of photons for the measurement, heavier atoms are used. This change flips the design of the traditional RLG-based INS, in that it uses light to capture and prepare atoms in a specific state whose interference patterns can be very accurately measured. By replacing photons with heavier atoms, sensitivity increases. This increase becomes clear when one notes that what the INS actually measures is a phase shift

$$\Delta\phi = \frac{2m}{\hbar}\boldsymbol{\Omega_{rot}} \cdot \boldsymbol{A} \tag{1.1}$$

where here m is the effective mass of our particle, $\boldsymbol{\Omega_{rot}}$ is a the rotation vector, $\hbar$ is the reduced Planck's constant, and $\mathbf{A}$ is the area of the interferometer [19].

Re-writing the above equation in terms of the minimum detectable rotation we see that $\boldsymbol{\Omega_{min}}$, The minimum detectable rotation

$$\Omega_{min} = \frac{\hbar\Delta\phi_{min}}{2mA} \tag{1.2}$$

is proportional to the effective mass of the atom of photon. Thus, by changing from the mass-less (that have very light effective mass) photons to the much heavier atoms we can see a corresponding increase in sensitivity. Indeed, as the mass of an atom being on average 10^4 MeV compared to the 1 eV effective mass of a photon, we can see that there is a potential decrease in the minimum detectable rotation rate of increase of:

$$\begin{aligned} \frac{\Delta\phi_{atom}}{\Delta\phi_{Photon}} &= \frac{m_{atom}}{m_{\gamma}} \\ &= \frac{10^4 * 10^6 eV}{1eV} \\ \frac{\Delta\phi_{atom}}{\Delta\phi_{Photon}} &= 10^{10} \end{aligned} \tag{1.3}$$

Although we see a 10^{10} mass increase (and corresponding potential sensitivity increase) over a photon based RLG, in practice due to real world limitations in design, most atomic gyroscopes 'only' see a 3-4 order of magnitude increase in sensitivity [20]. This more modest increase still represents a massive potential gain in the real world and is certainly worth pursuing.

1.3.1 The NPS Atomic Interferometer

The atomic gyroscope apparatus at NPS was designed by Dr. Frank Narducci and built by Commander Michael Manicchia (USN) between 2017-2020, and was a part of CDR Manicchia's PhD dissertation while at NPS [19]. Although designed from the beginning to be a dual beam gyroscope, time constraints prevented the assembly of the second atomic beam. Nonetheless, the apparatus is still novel in the realm of atomic interferometry due to its use of continuous light beams.

The majority of previous work in atomic interferometry has been done using pulsed light [9]. Light pulse atom interferometry allows for precise measurement of the atoms with the major advantage being the ability to distinguish between the two anti-parallel beams by adjusting the timing. The primary downside to this approach is that there are times when there is no measurement taking place (between pulses), resulting in a dead time where no rotation or acceleration is measured. Because of these dead times, this setup is not ideal for use in inertial navigation, where continuous updates are required. Therefore, the NPS apparatus was designed around an alternative method that uses continuous atomic and optical beams [20]. While continuous beam atom interferometers have been designed before [21], the NPS apparatus uses a number of novel approaches in design, including its

cooling and optical pumping setup (discussed in Chapter 2), as well as using rubidium-85, selected due to the fact that its transition frequencies match the operating frequency of common, inexpensive lasers [20].

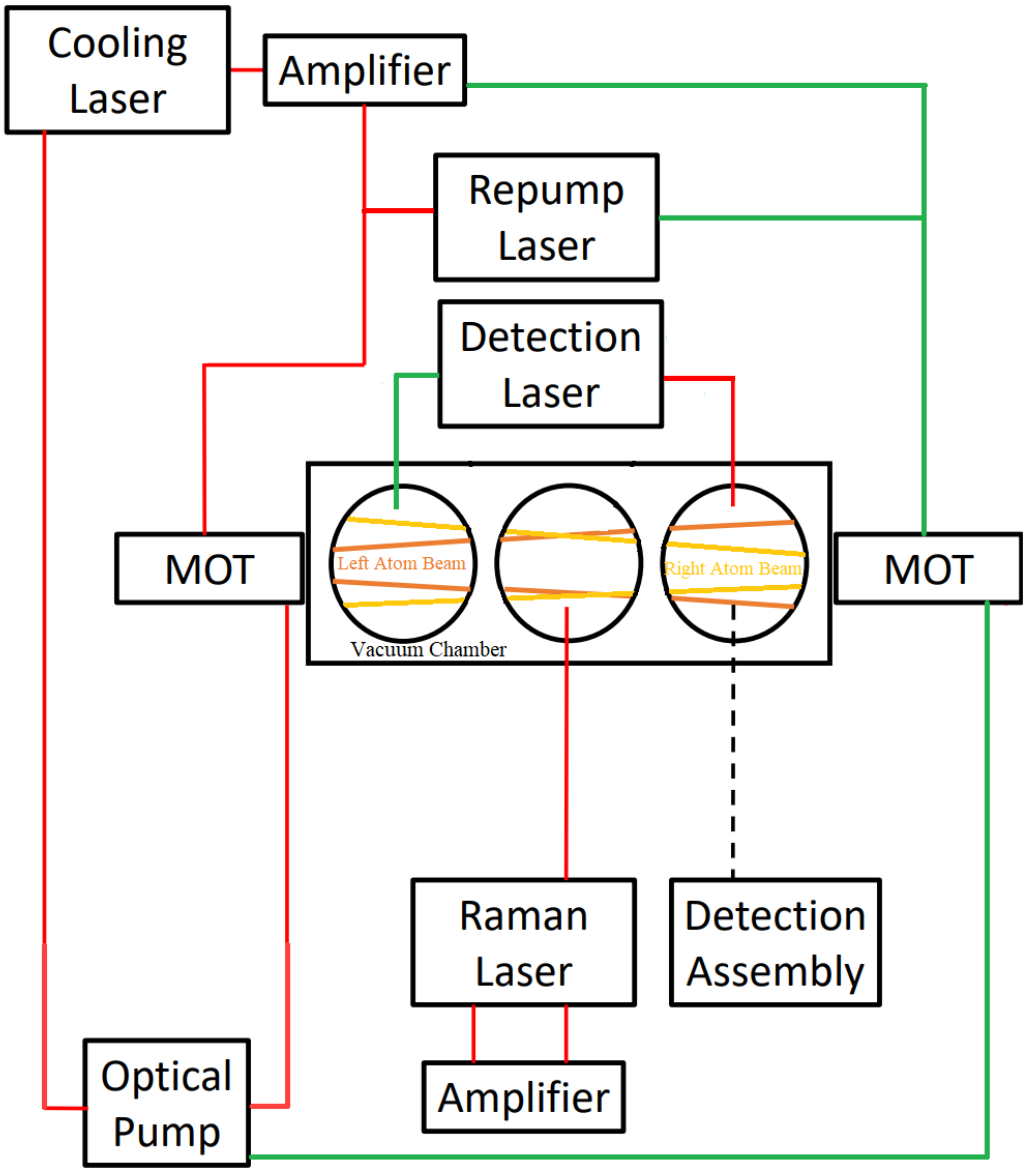

Figure 1.3. The block diagram of the current apparatus. Existing laser optics denoted by red lines. New laser optics created for this thesis denoted by green lines.

The NPS apparatus is functional but incomplete, lacking a second atomic beam. Without this beam,

the unit cannot distinguish between rotation and acceleration, which limits its use as a gyroscope. The objective of this research is to build upon the work already done on the NPS apparatus [19] by adding an anti-parallel atomic beam to allow for discrimination in rotation and acceleration, as well as improving the already existing design to improve efficiency. In this work, I will also discuss the challenges and potential solutions to bi-directional simultaneous measurement.

The summary of the rest of this paper is as follows. In Chapter 2, I discuss the background and theory behind the atomic gyroscope design and the decisions that lead to the current design of our apparatus. I will cover the construction and upgrades to the cage assembly and the associated optics in Chapter 3. In Chapter 4, I will present results of measurements I made demonstrating the improved performance. Finally, in Chapter 5, I will present my conclusions as well as discuss the work that remains for the future.

CHAPTER 2:
Background and Theory

This chapter will explain the foundation upon which my improvements to the apparatus are based, as it is important to understand how the system functions prior to any attempts at upgrades or changes. In this chapter, I will cover the background theory behind atomic interferometry, focusing on the design of the two-dimensional magneto optical traps that cool and trap atoms, which is the foundation of the research in this thesis. For completeness, I will also include a primer on state preparation and the theory behind detection and interferometry.

2.1 The Magneto Optical Trap

Atomic interferometry requires a stream of available cooled atoms in a well-defined state. The first step in the design of the apparatus is therefore the creation of this atomic beam. The solution lies in the two-dimensional magneto optical trap (2D-MOT), an assembly that uses lasers to cool and trap atoms in a known state and is key to our atomic interferometer design [19].

2.1.1 Laser Cooling

In order to understand the function of the 2D-MOT, we start with a simple two level atom. This atomic model has two energy levels that are referred to as the ground (G) and excited (E) state, with an energy difference between them (ΔE). We know from the Planck-Einstein relation that this energy difference can be expressed as a frequency, given by the equation $\Delta E = \hbar\omega_e$. Given this relationship, we can imagine a laser with a frequency ω_l, which is *less* than ω_e and the difference between the two is referred to as δ, ($\omega_l - \omega_e = \delta$). This difference between the two frequencies is known as *detuning*, or specifically where $\delta < 0$ *red-detuned*, and it is critical in the cooling of the atoms [22].

When this laser is applied to the atoms with zero velocity, there is a probability (given by Equation 2.1) that an incident photon will be absorbed by the atom and the atom will be promoted to the higher state.

$$P_e = \frac{\frac{1}{4}C_m^2/\beta^2}{\frac{1}{4}\Omega^2/\beta^2 + 1 + \delta^2/\beta^2} \tag{2.1}$$

Here, P_e is the probability of excitation, β is one-half the spontaneous rate of emission, δ is the detuning frequency, and Ω is the Rabi frequency. The Rabi frequency is the rate at which the atom cycles between states, and it depends on both the property of the laser used as well as the atom itself, given by the equation below:

$$\Omega = \frac{\mathbf{2}(\boldsymbol{\mu}^* \cdot \boldsymbol{\epsilon}_l)\varepsilon}{\hbar} \tag{2.2}$$

where $\bar{\mu}$ is the atomic dipole moment, $\bar{\epsilon_l}$ is the laser polarization vector and ε is the laser electron field amplitude. This process of changes in energy state through the absorption of photons is relevant for atomic cooling due to conservation of momentum. As we know from conservation of momentum, every time a photon is absorbed or emitted from an atom there is a corresponding gain or loss of momentum. When a photon is absorbed, the energy state changes and the atom gains a small kick of momentum, given

$$P = \hbar k = \hbar(\frac{2\pi}{\lambda}) = \frac{\hbar\omega_l}{c} \tag{2.3}$$

Here, P is our momentum, λ is the wavelength of the transition, with associated wave number k and c is the speed of light. From this formula, we can see that the momentum transferred by an individual photon is tiny. It is the cumulative effect of millions of these photons due to the fact that atoms can spontaneously emit photons at a rate of 2β which in the case of rubidium (for example) is $2 \cdot 2\pi(3Mhz)$. This has a pronounced effect on the atoms, imparting a significant momentum change.

The one-dimensional force imparted due to this momentum change is found by taking Equation 2.1 which gives the probability of excitation and multiplying by the momentum imparted per photon and the number of "kicks" per second controlled by the spontaneous emission rate, resulting in the following equation:

$$F = -(\hbar k)(2\beta)\left(\frac{\frac{1}{4}\Omega^2/\beta^2}{\frac{1}{4}\Omega^2/\beta^2 + 1 + \delta^2/\beta^2}\right) \tag{2.4}$$

The minus sign in front of the equation denotes that the force is *opposite* to the direction of the laser propagation.

This equation is only valid for stationary atoms. In our real-world experiment, the atoms are moving with some velocity distribution, and to account for this in our equation we must include a Doppler shift associated with atomic motion by modifying our frequency ω_l by $\pm kv$. A second laser cooling beam is used to to provide a Doppler shift in the opposite direction of the first. The resulting equation is:

$$F = -(\hbar k)(2\beta)\left[\left(\frac{\frac{1}{4}\Omega^2/\beta^2}{\frac{1}{2}\Omega^2/\beta^2 + 1 + (\delta - kv)^2/\beta^2}\right) - \left(\frac{\frac{1}{4}\Omega^2/\beta^2}{\frac{1}{2}\Omega^2/\beta^2 + 1 + (\delta + kv)^2/\beta^2}\right)\right] \tag{2.5}$$

which in the cases of small velocity v can be reduced to [22]:

$$F = -(\hbar k)(2\beta)\left[\left(\frac{\Omega^2}{\beta^2}\right)\left(\frac{k\delta/\beta^2}{\frac{1}{2}\Omega^2/\beta^2 + 1 + \delta^2/\beta^2}\right)\right] v \tag{2.6}$$

Because the repulsive force F is proportional to v, this effect has been termed 'optical molasses' .

While the above accurately describes the force imparted on the atoms by our cooling laser, it does not describe the process of cooling itself. To begin, we go back to the difference in energy between our excited state $\hbar\omega_e$ and the energy imparted by our cooling laser $\hbar\omega_l$. As we noted above, when the laser is *red-detuned*, $\omega_l - \omega_e$ is negative. In other words, after every absorption cycle the net energy gained by the atom is negative, and due to the conservation of energy that means the atom loses velocity / thermal energy. This combination of repulsive force and cooling results in the laser acting as a viscous medium for the atoms, creating the condition for *optical molasses* [22].

So far, we have described the cooling aspect but not the trapping aspect of a MOT. We will now discuss trapping of atoms.

2.1.2 Magnetic Trapping

The second primary function of a MOT is to localize (trap) atoms in a given region. This comes from permanent magnets arranged in an anti-Helmholtz configuration around the optical molasses, which cause the lasers to exert a force on the atoms that is proportional to position, rather than velocity (as we saw with the laser cooling) hence, the atoms become trapped.

The mechanism through which the magnetic fields accomplish trapping is the Zeeman shift of the magnetically sensitive sub-levels of the atom. This force is directly proportional to the distance of an atom from the "center" of the trap. For this process to work correctly, it is important that the optical cooling light is circularly polarized with either right or left handed circular polarization. Due to selection rules [19], the left handed light, $\hat{\sigma^+}$ will couple to the $\Delta m_F = +1$ sublevel and the right handed, $\hat{\sigma^-}$ couples to the $\Delta m_F = -1$ sublevel. The magnetic field has a linear profile near the center of the trap due to the anti-Helmholtz coils, as a result, the further 'off' an atom is from the center of our trap, the greater the Zeeman shift, and the resonance shifts closer to the red-detuned laser. Atoms to the right of center are shifted more into resonance with $\hat{\sigma^-}$ light, and further away from resonance with the $\hat{\sigma^+}$ light, resulting in a strong force pushing atoms back towards center. For atoms to the left of center, the reverse argument is true. The effect is the same on both sides—a force directing the atom back towards the center of the trap.

Figure 2.1 shows a graphical depiction of the process. One can see that the net effect of the cooling laser and opto-magnetic trap creates small region in which atoms will be concentrated into a smaller region.

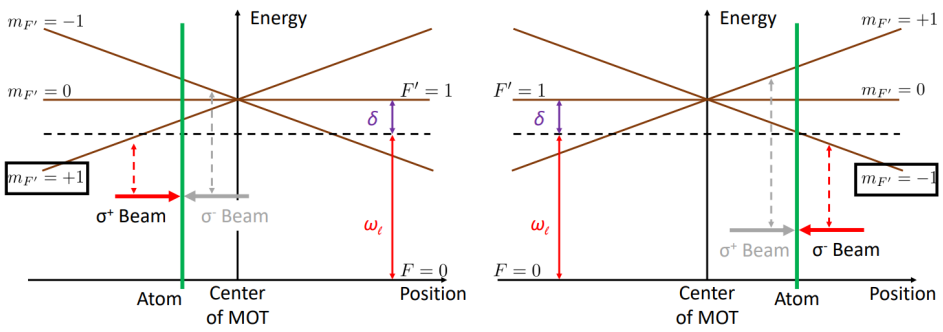

Figure 2.1. The force acting on the atom due to the right or left polarized light. Source: [19].

Mathematically, this can be included in a harmonic equation, by adding a resistive force Kx, where K is given by [22]:

$$K = \left(\frac{2\hbar k}{m}\right)\left(\frac{\Omega^2}{\beta^2}\right)\left(\frac{\delta}{(1+\delta^2/\beta^2)^2}\right) \tag{2.7}$$

The resulting harmonic equation becomes:

$$m\ddot{x} + b\dot{x} + Kx = 0 \tag{2.8}$$

2.1.3 Optical Pumping / Re-Pumping

When discussing the cooling, we used a simple two level atomic model; however, the level structure in rubidium-85 (^{85}Rb) used in the apparatus is a lot more complex. Our levels used are the $5S_{1/2}$ and $5P_{3/2}$ (See Figure 2.2). The transition between these two states is known as the D2 transition, which was selected as is corresponds to the wavelength of our laser used.

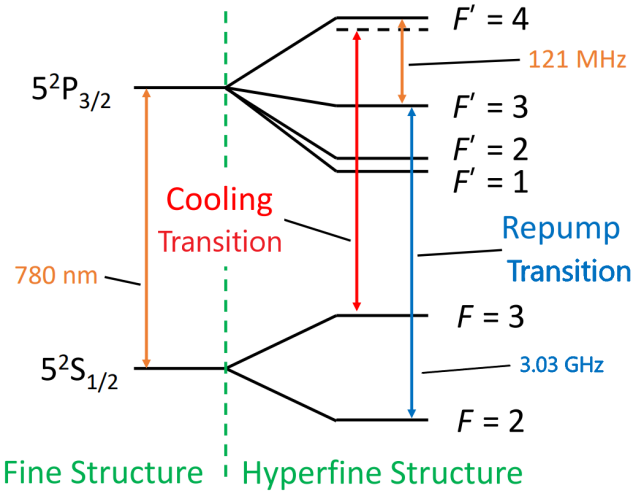

Figure 2.2. A view of the fine and hyper-fine structures of the rubidium 85 atom. Adapted from [19].

The "fine structure", J, corresponds to the orbital angular momentum L and the spin angular momentum S, whereas the "hyper-fine structure" adds the total nuclear angular momentum I.

$$Fine = \mathbf{J} = \mathbf{S} + \mathbf{L} \tag{2.9}$$

$$\text{“}Hyper - Fine\text{”} = \mathbf{F} = \mathbf{J} + \mathbf{I} \tag{2.10}$$

Our apparatus operates on the cooling transition between F = 3 and F' = 4 (the prime indicates an excited state). Due to the relative proximity of the F' = 4 and F' = 3, there is a nonzero possibility of the atom being excited to F' = 3 instead of F = 4. The actual probability comes from Equation 2.1,

where $\delta = 2\pi(121MHz)$, $2\beta = 2\pi(6.07MHz)$ [23], and $\Omega/\beta = 5$ (determined experimentally [19])

As $\Omega/\beta << \delta/\beta$, Equation 2.1 then reduces to:

$$\begin{aligned} P_E \text{ (F' = 3)} &\approx \frac{1}{\delta^2/\beta^2} \\ &\approx \frac{1}{(2\pi(121MHz)^2/(2\pi(6.07MHz))^2} \\ &\approx \frac{1}{1600} \end{aligned} \tag{2.11}$$

The result of this equation is that our apparatus has a 1/1600th chance of mistakenly exciting our ^{85}Rb atoms to the F' = 3 state instead of the correct F' = 4. While a 1/1600 change may not seem significant, given the number of cycles in this experiment it can drastically disrupt the process. The difference between F' =4 and F' = 3 that makes it so damaging to our experiment is that while selection rules prohibit F' = 4 from falling back into F = 2 (As ΔF must be 0 or ± 1), F' = 3 is a different matter and there is about a 50/50 chance [19] of an atom in the F' = 3 state falling back into the F = 2, from which our system is out of resonance and has no method of further cooling. With no solution to this issue, the cooling would stop at around 1600 cycles, and there would be no further cooling

A common solution is to add another laser, known as a *re-pump* laser, that is specifically tuned to the F = 2 to F' = 3 transition. This allows for another 50/50 chance at falling back into the correct F = 3 state. The atom has now been "re-pumped" back into the right level and the cooling process continues.

Once proper cooling is achieved, there is one final process in order to get our atomic beam into the vacuum chamber where we may conduct experiments. The cooled atoms in our atomic beam must all be in the correct F = 2 state when they enter the vacuum chamber. Placing the atoms into the F = 2 ground state involves another laser, known as the *optical pump* tuned to the F = 3 to F'= 2 transition. This transition was selected experimentally and due to advantageous branching ratios the decay from F' = 2 to F = 2 is four times more likely that F = 3 (see the full derivation in Appendix A).

2.2 Atomic Beam Interferometry

At this point, we have described the function and theory behind the 2D-MOT in our apparatus. The end result is an atomic beam of cooled atoms in the F = 2 state heading into our vacuum chamber. The next step in the apparatus is the atomic interferometry—that is the process in which Raman lasers act as both beam splitters and mirrors for the atomic beam. This method (known also as *Mach-Zehnder* type interferometer) has been used successfully with dual atomic beam interferometers using both temporally and spatially separated beams [12], [24]. This section describes the theory behind the single atomic beam interferometry and output detection of the apparatus. The challenges of simultaneous measurement when adding a second atomic beam path will be discussed in Chapter 3.

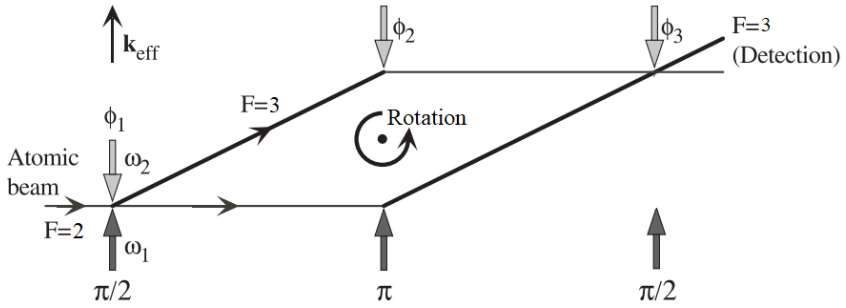

Figure 2.3. This figure shows a single beam model of atomic interferometry with the three Raman pulses indicated and the associated energy states of the atoms. Adapted from [24].

2.2.1 Stimulated Raman Transitions

A Raman process is one by which an atom starts in one state and then ends up in another. In this apparatus our Raman process is a stimulated one, where two lasers are stimulating the transition between the states. This process is used because it facilitates the transition between two atomic states with no spontaneous incoherent emissions, as will be explained below.

A simplified version of the process can be envisioned as involving three level atom with two ground states and one excited state and also involves two lasers, one of which has a frequency ω_1 and excites from one ground state (|1> which corresponds to F = 2) to an excited state (|3> or F'). The other laser is tuned to ω_2 and excites the second ground state (|2> or F = 3) to that same excited state (|3>).

Figure 2.4 depicts this interaction of a three level atom in a *Lambda Configuration*, named for its

shape [20]. Here, the individual laser detuning from their respective transitions are represented by δ_1 and δ_2, and the difference between our ground states |1> and |2> is represented by Δ, and is also called *Ground-State Hyperfine Splitting*.

Recalling our Rabi frequency Equation 2.2, with two lasers we end up with two Rabi frequencies, corresponding to:

$$\Omega_1 = \frac{2(\boldsymbol{\mu}^*_{\mathbf{13}} \cdot \boldsymbol{\epsilon}_{\boldsymbol{l}})\varepsilon_1}{\hbar} \tag{2.12}$$

and

$$\Omega_2 = \frac{2(\boldsymbol{\mu}^*_{\mathbf{23}} \cdot \boldsymbol{\epsilon}_{\mathbf{2}})\varepsilon_2}{\hbar} \tag{2.13}$$

where $\mu_{13}(\mu_{23})$ is the dipole moment of the $1 \rightarrow 3(2 \rightarrow 3)$ transition, $\epsilon_1(\epsilon_2)$ is the first (second) laser polarization and $\varepsilon_1(\varepsilon_2)$ is the first (second) laser amplitude, associated with the lasers driving from |1> to |3> and from |2> to |3>, respectively.

To achieve a stimulated Raman process, each laser is detuned from the excited state such that $\delta_1 = \omega_1 - \omega_{13}$ and $\delta_2 = \omega_2 - \omega_{23}$. δ_1 and δ_2 are chosen such that $\delta_1 - \delta_2 - \Delta \approx 0$. This will put the system close to two photon resonance. However, δ_1 and δ_2 are each individually chosen to be large.

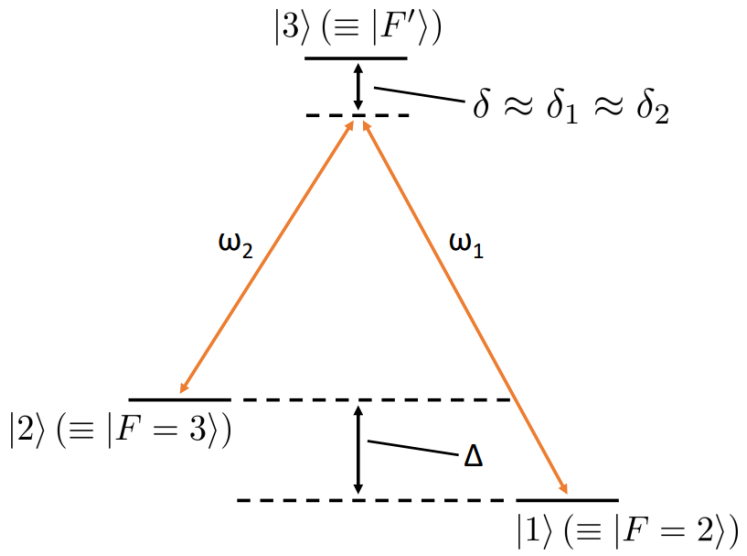

Figure 2.4. A three level atom in a lambda configuration. Source: [19].

The end result is a Raman process, where the transition from the |1> to |2> state takes two photons in a two-step transition using |3> as an intermediate state. As the atoms spend very little time in the |3> state, effectively we have a virtual transition back and forth between |1> and |2>, the two ground states, with no spontaneous emissions to worry about. As a result, we can consider our |1> state a ground state (denoted |g>) and our |2> state our new excited state (denoted |e>). The interaction between these states is what forms the basis of our interferometry measurements.

In a *Mach-Zehnder* interferometer design, there are three laser injection regions used, each with its own Raman pulse. These Raman pulses are described as either $(\pi/2)$ or (π) pulses depending on their use. The first injection region is the first $(\pi/2)$ pulse, which acts as a beam splitter, creating a superposition of F = 2 and F = 3 ground states. The beam then passes through a (π) pulse, also called an atomic mirror, exchanging the atomic states and deflecting the trajectories back towards each other. The final region is another $(\pi/2)$ pulse, which combines the beam into one coherent output beam. See Figure 2.3 for a view of this process.

Rotation is observed by noting a phase shift between the two paths, due to the Sagnac effect, similar to the RLGs in Figure 1.1. This effect will be discussed further in Section 2.3.

2.2.2 Detection

Detection of the final state of the atoms in the beam is handled by a detection laser tuned to the F = 3 to F' = 4 transition. Any atom in the F = 3 state will interact with this laser, exciting to the F' = 4 state before decaying back into the F = 3 state and this florescence can be detected and measured. Any atom that is not in the F = 3 state will pass through this laser without interaction. Thus, the ability to detect rotation and acceleration by the apparatus depends on the ability to measure all the atoms in the F = 3 state.

However, the cooling and re-pumping process leaves all almost all the atoms leaving the cell in the F = 3 state. This means that leaving them in this state means we are unable to measure any meaningful interactions between path lengths, and we will be unable to perform any experiments. The solution to this issue is to put the atoms back into the F = 2 ground state prior to leaving the cell and entering the vacuum chamber, which is the function of the optical pumping laser as described in Section 2.1.3.

2.3 Dual Beam Theory and Distinguishing between Rotation and Acceleration

The resulting fundamental output from our system as described so far is a measurement of the number of atoms in an excited state. With a single atomic beam system, the interferometer will acquire a phase shift, either due to acceleration or rotation or a combination of both [20], [24].

A phase shift due to acceleration is given by

$$\Delta\phi_{acc} = k_{eff}\alpha T^2 \tag{2.14}$$

where α is the acceleration, T is the time between light pulses, and k_{eff} is the effective laser wave number.

A phase shift due to rotation is in the form:

$$\Delta\phi_{rot} = \frac{2m}{\hbar} 2\mathbf{\Omega} \cdot \mathbf{A} \tag{2.15}$$

where $\mathbf{\Omega}$ is the rotation vector. An abbreviated derivation for both of the above terms can be found in Appendix B.

The total phase shift will be a combination of these two individual phase shifts.

$$\Delta\phi_{tot} = \Delta\phi_{rot} + \Delta\phi_{acc} \tag{2.16}$$

With a single beam based system, there is no way to distinguish the individual contributions of rotation and acceleration towards the total phase shift. Unless one has external knowledge of the motion of the system, there is no way to separate a rotation based phase shift from an acceleration based one and one is instead left with only the ambiguous total phase shift.

The solution to this problem is to add a second, anti-parallel beam to the system. The addition of such a beam results in two interferometers with two area vectors, $\mathcal{A}$, where each will have a direction given by the direction of the atom' travel crossed with the laser wave vector of our Raman laser ($\bar{v} \times k$). The area vectors of the two beams will be then nearly identical, and only differ by a sign for the same direction of rotation.

With all else being equal in the formula, when we add the total phase shifts for each interferometer, the combinations due to rotations will cancel out, resulting in a phase shift due to acceleration only. Furthermore, when we subtract the total phase shifts, we end up with the pure rotation result

$$\begin{aligned}
\Delta\phi_{beam1} + \Delta\phi_{beam2} &= \Delta\phi_{acc1} + \Delta\phi_{rot1} + \Delta\phi_{acc2} + \Delta\phi_{rot2} \\
&= \Delta\phi_{acc1} + \Delta\phi_{acc1} + \Delta\phi_{rot1} + \Delta\phi_{rot2} \\
&= k_{eff}\alpha T^2 + k_{eff}\alpha T^2 + \frac{2m}{\hbar}2\Omega \cdot \mathcal{A}_1 + \frac{2m}{\hbar}2\Omega \cdot \mathcal{A}_2 \\
&= k_{eff}\alpha T^2 + k_{eff}\alpha T^2 + \frac{2m}{\hbar}2\Omega \cdot \mathcal{A}_1 - \frac{2m}{\hbar}2\Omega \cdot \mathcal{A}_1 \\
&= k_{eff}\alpha T^2 + k_{eff}\alpha T^2 \\
&= 2k_{eff}\alpha T^2 \\
&= 2\Delta\phi_{acc}
\end{aligned} \tag{2.17}$$

$$
\begin{aligned}
\Delta\phi_{beam1} - \Delta\phi_{beam2} &= \Delta\phi_{acc1} + \Delta\phi_{rot1} - \Delta\phi_{acc2} - \Delta\phi_{rot2} \\
&= \Delta\phi_{acc1} - \Delta\phi_{acc1} + \Delta\phi_{rot1} - \Delta\phi_{rot2} \\
&= k_{eff}\alpha T^2 - k_{eff}\alpha T^2 + \frac{2m}{\hbar}2\Omega \cdot \mathcal{A}_1 - \frac{2m}{\hbar}2\Omega \cdot \mathcal{A}_2 \\
&= \frac{2m}{\hbar}2\Omega \cdot \mathcal{A}_1 + \frac{2m}{\hbar}2\Omega \cdot \mathcal{A}_1 \\
&= 2\frac{2m}{\hbar}2\Omega \cdot \mathcal{A}_1 \\
&= 4\frac{2m}{\hbar}\omega \cdot \mathcal{A}_1 \\
&= 2\Delta\phi_{rot}
\end{aligned}
\tag{2.18}
$$

Therefore, it is the addition of the second anti-parallel beam path that allows for the creation of an atomic gyroscope, and allows the accurate and separate measurement of both rotation and acceleration that is required for any inertial navigation system.

CHAPTER 3:
Design and Construction of Second 2D-MOT Laser Optics Cage Assembly

In this chapter, I will cover the design and construction of the second 2D-MOT cage assembly, which allows for the anti-parallel atom beam generation. This cage assembly generates a second atomic beam anti-parallel to the first, bringing with it the capability to distinguish between rotation and acceleration to the apparatus. I will also address functional design considerations, including upgrades over the original baseline cage assembly. As the system was only set up for one atomic beam, I will discuss the required splitting of the optical pump and detection laser assemblies to allow for bi-directional measurement.

3.1 Existing Cage Assembly

Prior to the construction of the second cage assembly, the apparatus consisted of a single cage assembly to house the MOT laser optics and create the MOT, a rubidium cell, connected via a pinhole aperture to a 9-inch long vacuum chamber, typically kept at $1.9X10^{-9}$ torr.

The vacuum chamber has 12, 2.75 inch ConFlat^{TM} windows (three per each of the top, bottom, front, and back sides of the vacuum chamber) that are used or blocked off as required to subject the atomic beams within to the various types of light required to perform a given experiment. On each side of the vacuum chamber is a rubidium cell. For ease of description going forward, the existing cage assembly side will be arbitrarily referred to as the "left side" of the apparatus, while the new cell assembly will be referred to as the "right side".

While the atomic interferometer apparatus was conceived and designed to allow for two anti-parallel atomic beams, time constraints in the original construction allowed for only one of the cage assemblies, and therefore beam, to be set up. The existing cage assembly was constructed around a 30mm standard cage size, allowing for 1 inch (25.3mm) optics throughout.

3.1.1 Components

The existing cage assembly is composed of four basic components: 1) fiber couplers; 2) half wave plates; 3) quarter wave plates; and 4) polarizing beam splitters. Each component is described

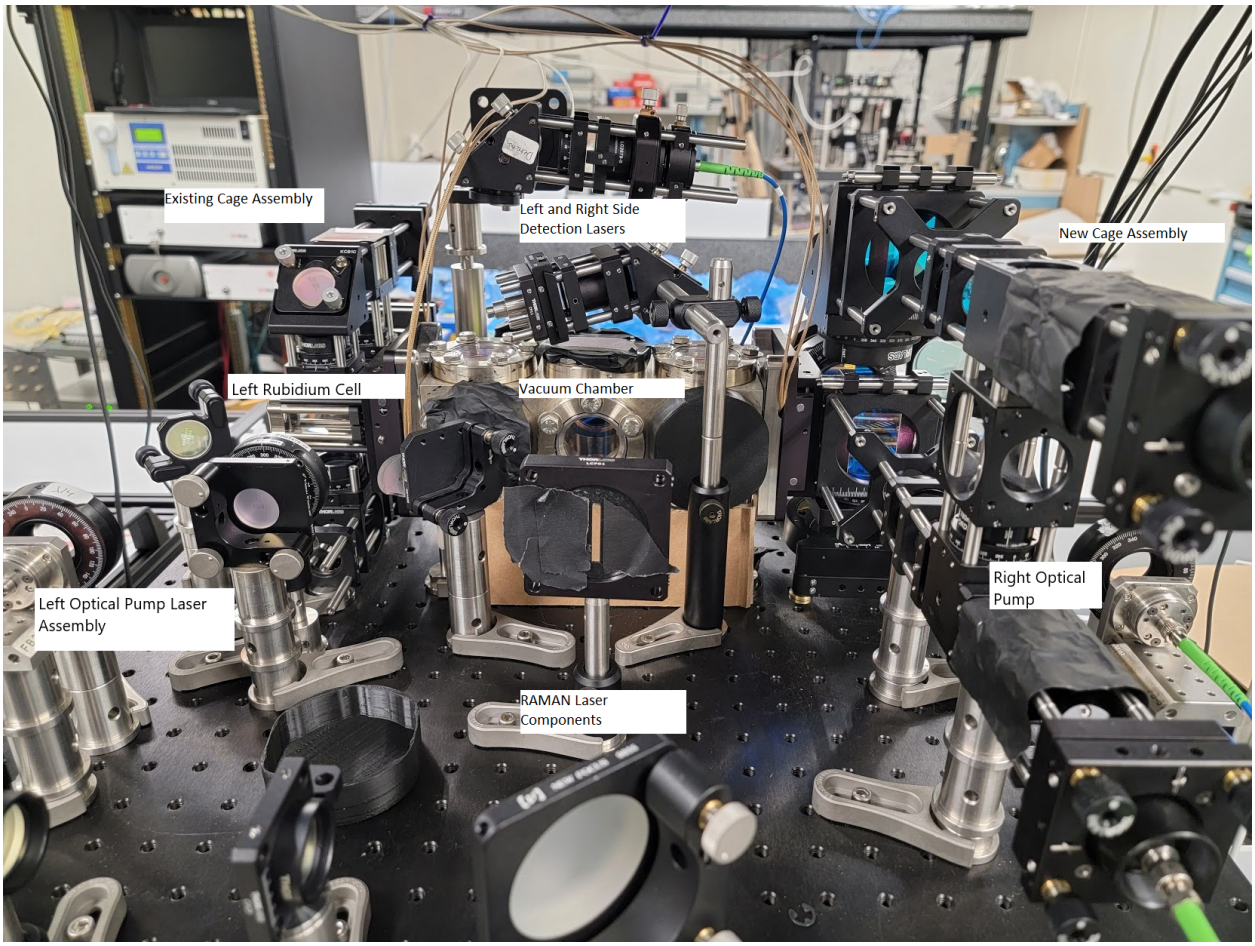

Figure 3.1. Commented photograph of the apparatus and dual cage assemblies

briefly below.

3.1.2 Fiber Coupler

The fiber coupler component holds the output side of a fiber containing laser light. As the output from the fiber terminal is not focused or collimated, in the existing cage assembly it is followed by a lens assembly that provides focusing and collimation.

3.1.3 Half-wave Plate

Half-wave plates (HWP), also referred to as a $\frac{\lambda}{2}$ plates, rotate the polarization vector of any light that passes through it. Linearly polarized light is rotated about the major axis of the wave plate, whereas any circularly polarized light that passes through the plate is rotated through elliptical polarization to circular polarization of the opposite handedness. Within this assembly, the $\frac{\lambda}{2}$ wave

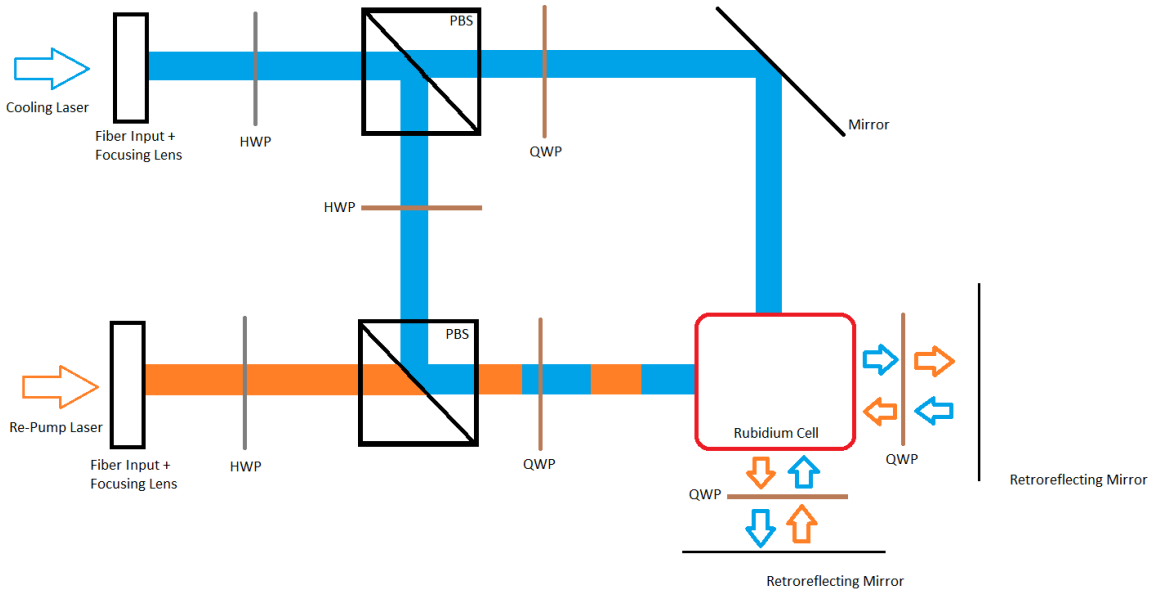

Figure 3.2. The existing cage assembly functional diagram

plates are used to control the intensity of the light that enters the cage from both the cooling and re-pump laser assemblies. For the cooling laser, the HWP is used to control the polarization of the light entering a polarizing beam splitter. Since the beam splitters separate the beams of light based on polarization, and since the HWP controls the percentage of cooling light in each polarization state, ultimately rotating the HWP controls the cooling laser light split between the vertical and horizontal path. In the re-pump path, by rotating the HWP, one can "block" the light by polarizing it in a manner that will get reflected out of the assembly by the lower polarizing beam assembly, allowing for precise control of laser re-pump laser intensity.

3.1.4 Quarter-wave Plates

Quarter-Wave Plates (QWP), also referred to as a $\frac{\lambda}{4}$ plates, change the polarization of any light that passes through from linear to circular polarization or back the other way. In this apparatus the QWP are used to convert the linearly polarized light into the correct circular polarization as required to cool the atoms in the Rubidium cell, as discussed in Section 2.1.

3.1.5 Polarizing Beamsplitter

The Polarizing Beamsplitter (PBS) splits any incoming laser beam into two paths: horizontally polarized light is transmitted and vertically polarized light is reflected. Each path is based on the polarization of the light entering. Thus, if there is a laser beam that consists of light that has both vertical and horizontal linearly polarized components, the vertically polarized portion will be directed to one path and the horizontally polarized component will be split off in the other. In the apparatus, the top PBS is used to split the cooling laser into a horizontal and vertical path, whereas the bottom PBS is used to control the intensity of the re-pump light entering the chamber by reflecting any unwanted light out of the assembly.

3.1.6 Construction

The cage itself consists of two laser fiber inputs, one for the cooling and one for the re-pump lasers, as discussed in the previous chapter. The light beam exiting the fibers are collimated by lens assemblies and then pass through HWPs that allows for precise control over how much light from each laser is transmitted through the rest of the cage. The laser light from both sources are then combined by two polarizing beam splitters and then correctly polarized again with a QWP. The right and left circularly polarized components then enter the cell from their respective orientations, pass through the cell and then pass through another QWP before getting retro-reflected back towards the cell. The functional diagram can be seen in Figure 3.2

Characteristics

The advantage of the existing MOT laser optics cage design was in its compact nature; however, the downside was the resulting laser beam sizes were small in comparison to the rubidium cell size. The laser beams were collimated to a size of approximately 8mm diameter which needs to be contrasted with the cell size 20mm x 60mm. It was this downside that the new cage assembly was designed to improve.

For a complete breakdown and characterization of the atomic beam formed by the original cage assembly, see [19].

3.2 Design of New Cage Assembly

In planning for the new design of the cage assembly, the goal was first to incorporate a number of design changes to improve the performance of the cage. The primary design change was to increase the beam size of both the cooling and re-pump lasers as they entered the rubidium

cell. The existing cage assembly relied on the natural divergence of light coming out of the fiber connector and collimated the light with a single lens. The new cage design incorporates both a larger collimator package as well as a telescoping lens package in both arms of the cage assembly to achieve a much larger coverage of the cell.

The bulk of the design changes centered around the expansion of both cooling and re-pump beams to cover a much larger portion of the rubidium cell. The first step in the beam expansion is the collimator, which takes the output of the fiber (either cooling or re-pump), and expands the beam to an 8mm diameter. This replaces and improves on the lens focusing assembly in the original cage design, as the coherent laser beam that emerges is much larger and more coherent than the laser in the original assembly, which relied only on a focusing lens to achieve the same result. This new collimator ensures that our beam is almost as large at the collimator output as the original beam is at the MOT cell.

The 8mm diameter collimated beam is then passed through the same HWP and PBS setup that was found on the existing cage. However, the next design change involves a telescoping lens section, consisting of a -25mm focal length bi-concave lens, followed by two cylindrical lenses, of 50mm and 150mm focal lengths. The result is a beam that diverges to 16 x 50mm, which is 85% of the area of the cell, before any other natural beam divergence effects. This also results in an oval beam pattern that can more effectively fill the required dimensions without a major light loss outside the bounds of the cell.

The second design change is the addition of a beam sampler to the laser line. Locating the sampler directly after the collimator output, allows for more convenient ability to read the output laser power without having to block the beam. This change allows for quick beam power measurements, and is a useful addition to the cage assembly.

The cage design follows the same template as the original cage, with two fiber inputs, HWP to control light input from the two lasers into the cage, followed by polarizing beam splitters. The telescoping optics are then placed after the polarizing beam splitters.

3.3 Construction of New Cage Assembly

The construction of the new cage assembly was done in concert with a swap to a larger "breadboard" work surface under the assembly. This change was motivated in part to the larger size footprint of the newer cage assembly, as well as the increased size requirements from having to duplicate both the detection and optical pumping laser assemblies. This change necessitated the removal of the

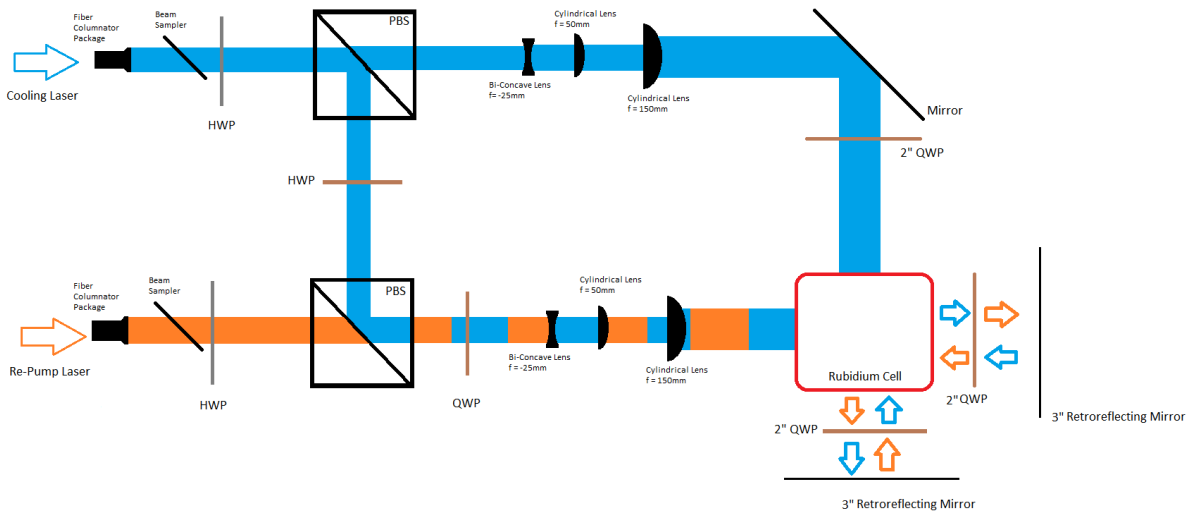

Figure 3.3. The new cage assembly functional diagram

rotation stage, which granted more headroom in the apparatus by lowering the work surface.

The addition of the telescoping lenses to the cage assembly resulted in a much larger assembly then the existing cage. The larger beam size necessitated using 2 inch optics in the cage, with 3 inch retro-reflectors after the cage assembly. This design change resulted in the addition of a 60mm assembly components near the laser output side of the cage assembly, and required much larger QWPs and retro-reflectors after the cage. The larger physical size of the cage assembly can be seen Figure 3.4. Even with the larger work surface it was a challenge to fit the cage as well as the optical pump laser assemblies on the work surface and it resulted in a much tighter clearance to get the new optical pump assembly aligned correctly. Once installed, clearance issues with the telescoping lens assembly resulted in the left and right portions of the oval beam being cut off, and as a result the beam entering the rubidium cell has a rectangular aspect ratio as seen in Figure 3.5.

3.4 Designing for Dual Atomic Beam Operation

In order to conduct dual beam simultaneous measurements, the existing optical pump and detection laser assemblies needed to be split into two. The existing assemblies were only set up on the left side of the cage side and provided for unidirectional measurement only.

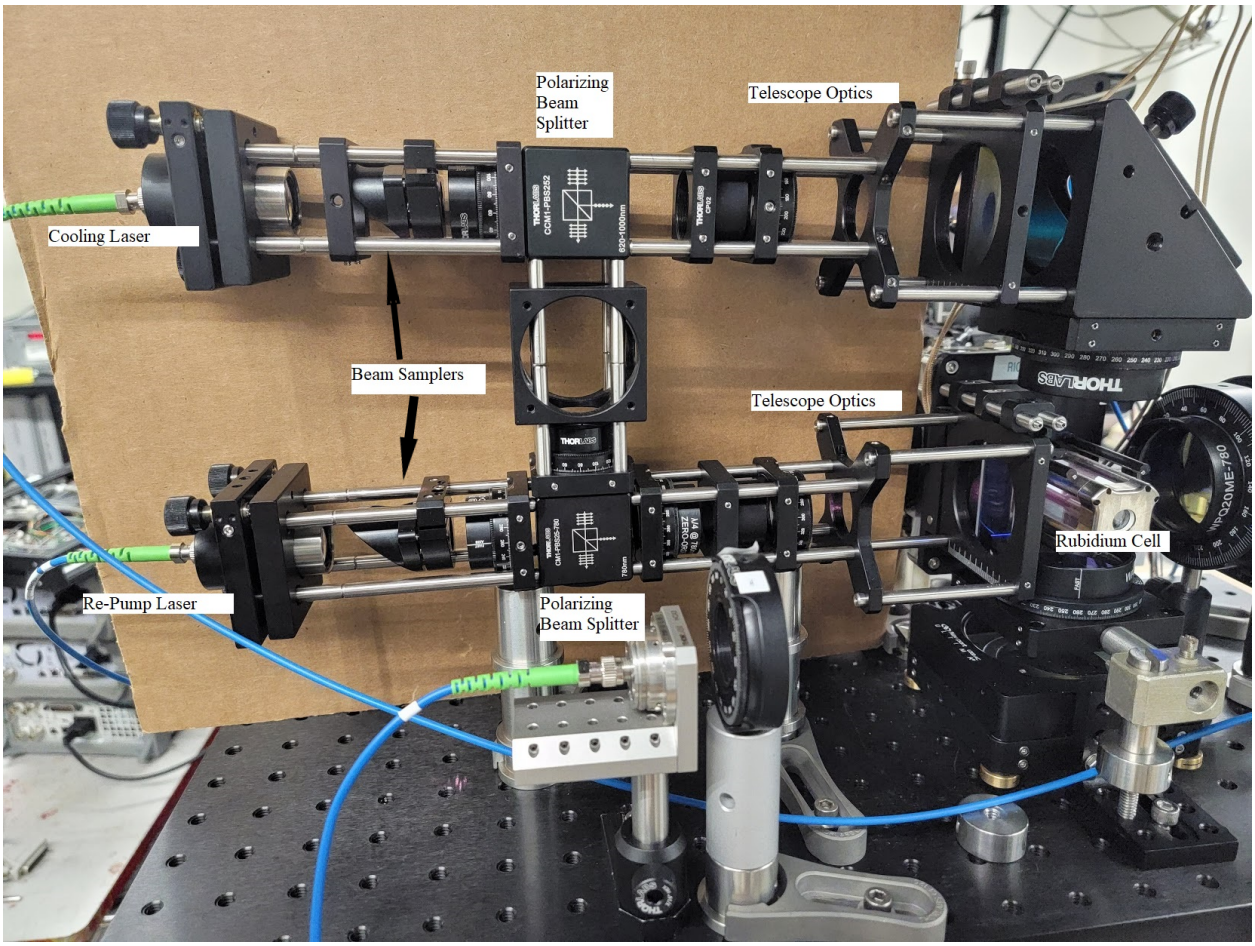

Figure 3.4. Annotated photograph of the new cage assembly. Includes the new optical pump assembly in the foreground

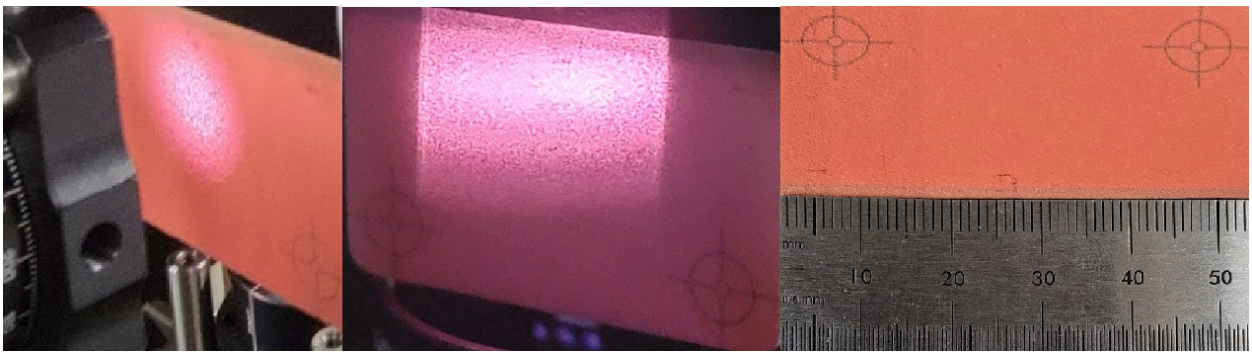

Figure 3.5. Comparison of beam spot sizes, beam from existing left side cage assembly on left, new beam formed by new right side cage center, and scale on right

3.4.1 Changes to the Detection and Optical Pump Assemblies

Both detection assemblies provide a collimated output beam sheet used to fluoresce any atoms in the upper ground state (F = 3), but the new detection laser assembly incorporates some design changes to improve the packing and to simplify the optical path. Reducing the physical footprint of the detection laser apparatus better allows for both assemblies to be on at once without any physical interference.

The new assembly consists of an integrated fiber columnator that is both smaller physically, and a simpler optical set up, than the legacy detection laser assemblies multiple lens system. The detection assemblies are then physically stacked, one detecting on the left side of the assembly and the other on the right (see Figure 3.6 for physical layout).

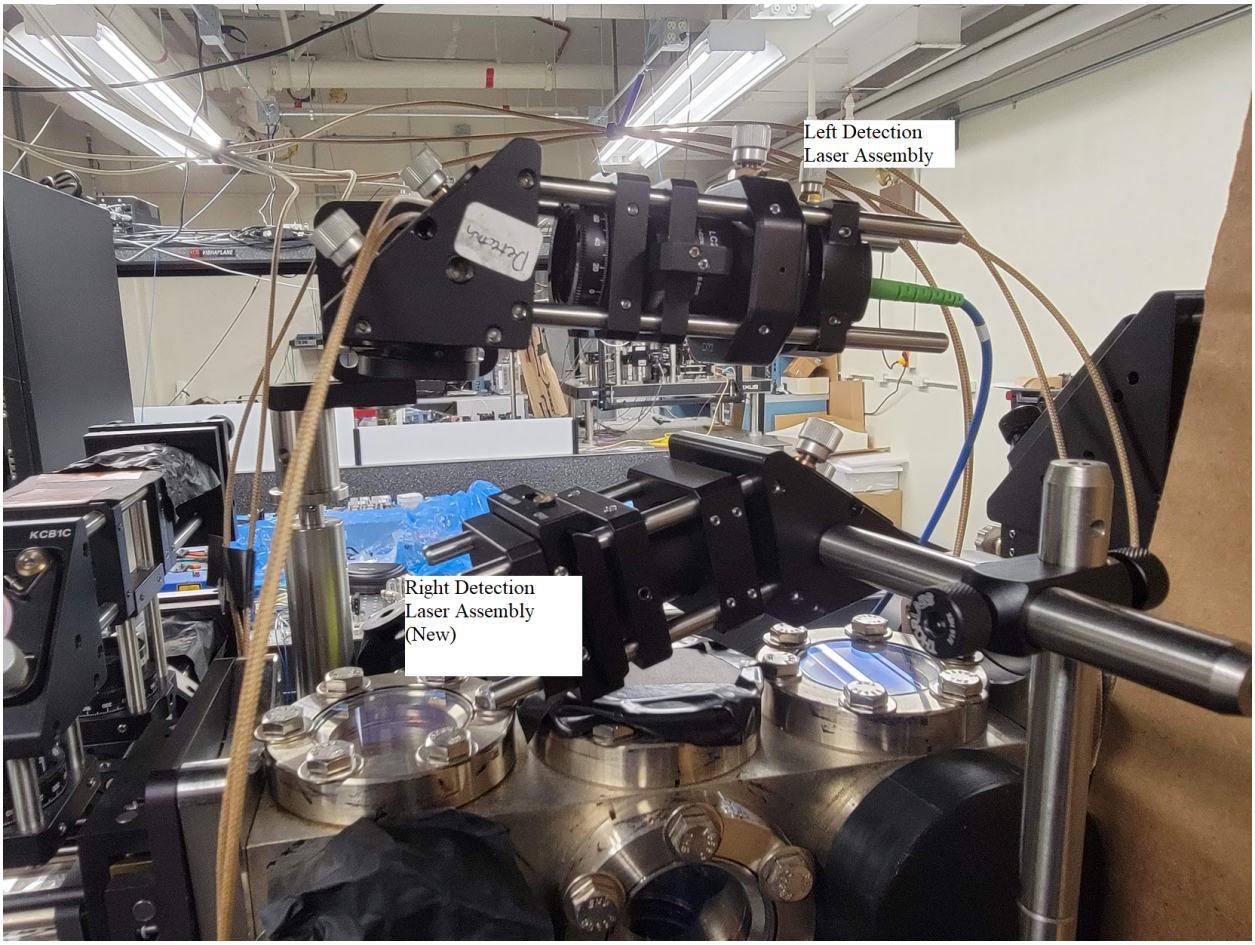

Figure 3.6. Dual detection laser setup. Existing (left side) detection laser on top, and the new (right side) assembly on bottom

The splitting of the optical pump assembly was straight-forward. A 1 to 2 fiber splitter was used

and the existing optical pump assembly (consisting of a fiber coupler, QWP and mirrors to direct the beam into the cage) was mirrored on the new cage side of the assembly. The only design consideration was due to space considerations, as the mirror assembly that guides the optical pump laser into the right hand cell was moved to the very outside of the working surface in order to fit the smaller available footprint on the new cage assembly side.

3.4.2 Dual Beam Measurement

The end result of these changes is a system that is designed to allow for simultaneous measurement from both atom beams. As the system uses continuous beams of atoms, as opposed to the pulsed atom beams more common in existing atomic gyroscopes [24], the timing based measurement systems used in other systems do not work. The challenge when conducting measurements with both atom beams at the same time is avoiding any cross talk between beams. As the detection lasers are continually operating, they cannot distinguish between atoms in the F=3 state that are just leaving the aperture closest to them from those F=3 atoms that have left from the farther aperture and have crossed the vacuum chamber. As the measurements require precise measurement of the interference patterns in both beams simultaneously but separately, this poses a challenge with our continuous beam operation.

The solution is to set our optical pumping and detection beams as laid out in Figure 3.7. The optical pumping lasers ensure that all the atoms that leave each cell are in the dark (F=2) state, where they can pass through the "close" detection laser without interaction. Once they pass through the Raman laser beam in the center window however, some atoms will be transitioned to the F=3 state, and these atoms, still traveling away from their respective rubidium-85 cells, will then pass through the detection laser, leading to a fluorescence that can be measured with a photo multiplier tube (PMT), a sensor that detects fluorescence caused by atomic interaction and converts it to an electrical signal that can be displayed on an oscilloscope. This setup has not yet been experimentally tested.

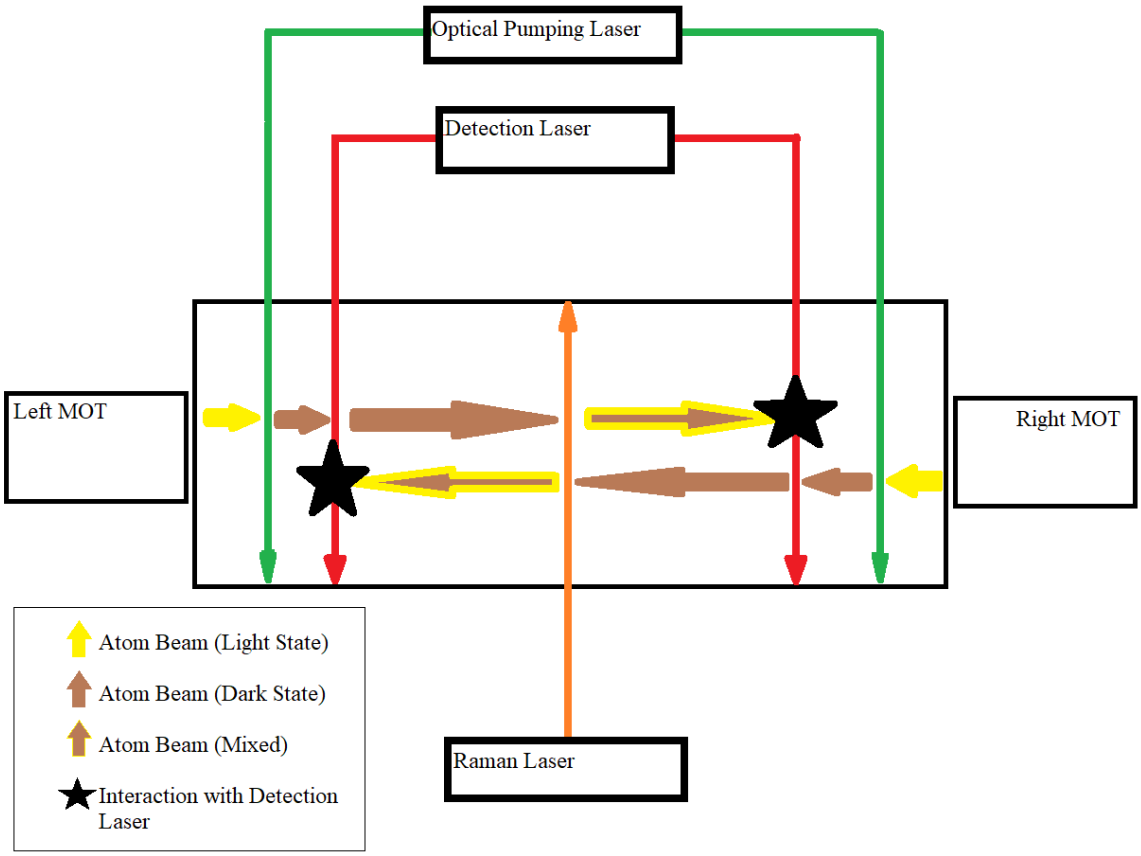

Figure 3.7. Functional diagram of the simultaneous dual detection/optical pumping setup. After being optically pumped, each beam passes without interaction through the closer detection beam before interacting with the Raman beam and then interacting with the far detection beam.

CHAPTER 4:
Characterization of Second Atomic Beam: Experiment

In this chapter, I will discuss the results obtained in characterizing the second atomic beam formed by the laser optics in the new cage assembly, including experimental procedure and characteristics obtained.

4.1 Initial MOT Set up

Once the new cage assembly construction was finished and installed on the left side, the initial challenge was to achieve a MOT. The re-pump and cooling laser fibers were brought from the existing (left side) to the new cage assembly on the right side, in order to characterize the new atomic beam without any interference from the existing atomic beam.

The detection and optical pumping assemblies were duplicated as discussed in the previous chapter, but only one side was used for the initial characterization experiments.

The initial MOT set up went quickly, leading to results on the fluorescent CCD camera (Mightex CCE-B013-U USB) within an hour of powering up and locking the laser frequency at the appropriate frequency, as seen in Figure 4.1. It was theorized that the much larger beam size of the new assembly resulted in a much larger "Sweet Spot" in the creation of a MOT than the previous assembly.

The generated MOT appeared very bright on the CCD, indicating the presence of a great number of atoms, however, there was no signal at the PMT—indicating that the MOT was not aligned correctly with the aperture and there was no atoms leaving the cell. After adjusting the magnets located around the cell to move the location of the MOT within the cell, a strong signal was detected at the PMT (shown in Figure 4.2) and the characterization of the atomic beam could begin.

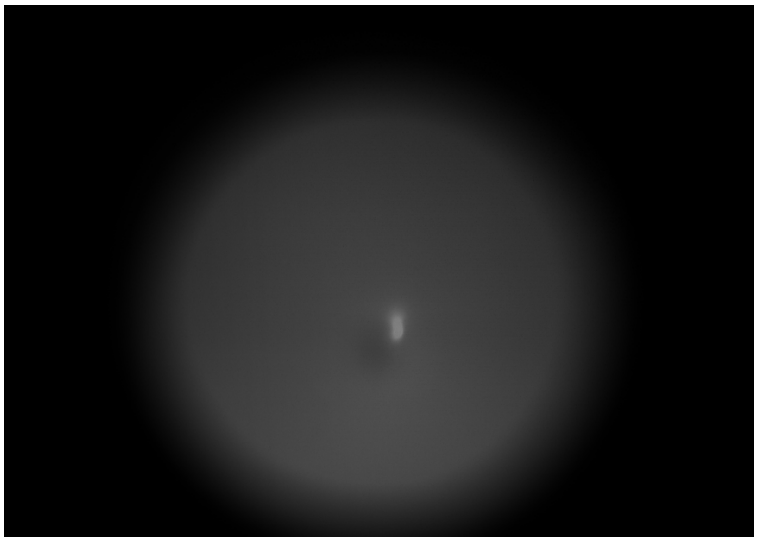

Figure 4.1. The first MOT achieved with new cage assembly.The bright fluorescence spot indicates the presence of trapped atoms. The dark spot near center of the cell is the aperture.

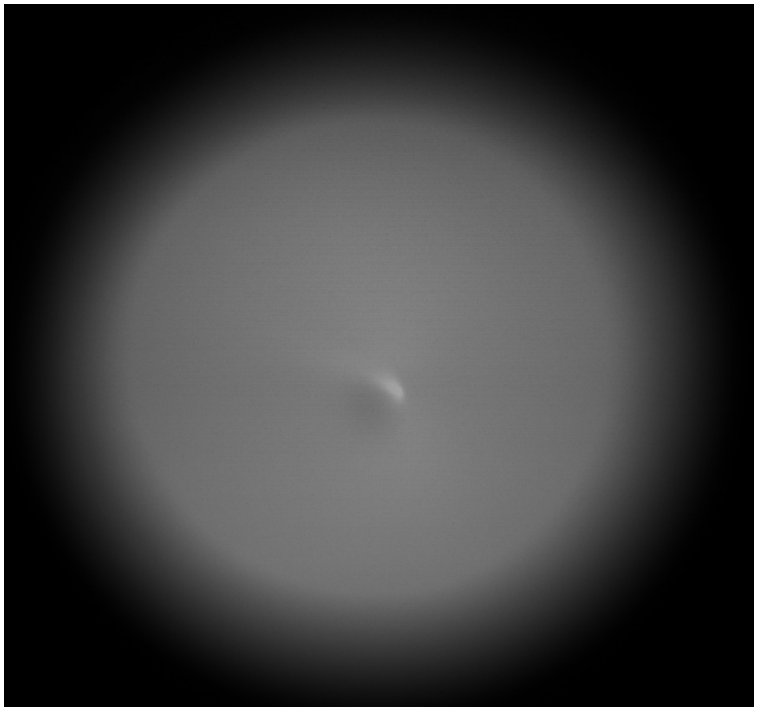

Figure 4.2. A typical picture after the MOT location was spatially aligned with the aperture within the cell. The MOT itself is slightly more diffuse and its location relative to the aperture was experimentally found to give the highest signal strength.

4.2 New Atom Beam Characterization

The key metric in determining the strength of the MOT is the fluorescence from the atomic beam. As the atom beam travels from the aperture down the long axis of the vacuum chamber, it interacts with the detection laser (Eagleyard EYP-DFB-0780-00080-1500-TOC03 distributed feedback laser) as it passes through the far window from the aperture. In our atom beam, those atoms in the F = 3 state will excite to the F' = 4 state before the majority of the atoms will decay back to F = 3 (as described in Section 2.2.2) giving off fluorescence that is then detected by the PMT (Hamamatsu H6780-20). The signal received is a Lorentzian (see Figure 4.3 for a typical example), and the intensity of the peak is correlated to the number of atoms in the beam and therefore the strength of the MOT itself. It is from this measurement that the beam can be optimized, using a measurement of signal above background (SAB) or signal to noise (SNR).

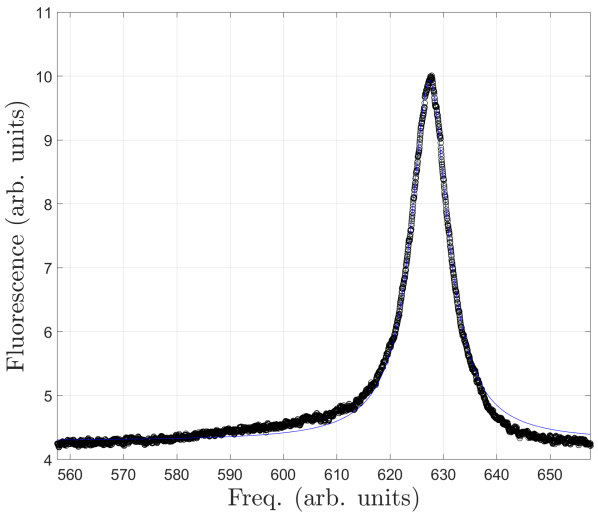

Figure 4.3. Typical Lorentzian signal received at the PMT. Data (in black) shown against Lorentzian curve fit in blue

In order move towards being able to conduct dual beam experiments, the new atom beam will need to be fully characterized. As the rubidium cell had never been used prior, we started by looking at the performance characteristics of the cell itself, before moving towards characterizing the beam itself, as well as looking at the performance of the updated detection laser and optical pumping assemblies when applied to the newly created cooled rubidium beam.

4.2.1 Rubidium Cell Optimization

In order to determine the performance of the rubidium cell used, we first achieved a functional 2D-MOT using "standard" cell current and laser power settings derived from the existing cell and the fluorescence from a scanning detection laser was collected. The cell current was adjusted and then varied between 2 amps to 2.6 amps. The results were plotted against SAB as shown in Figure 4.4 in order to find the optimum level of the current required to get the highest SAB before the system reached saturation point and the degradation of the 2D-MOT signal.

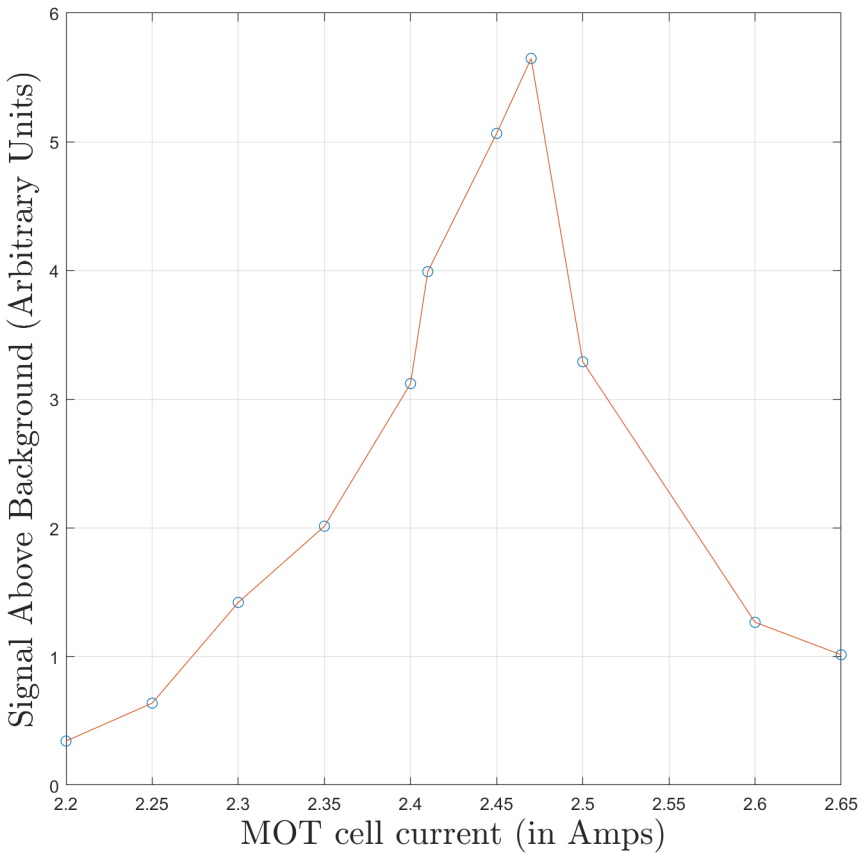

Figure 4.4. Plot of cell current versus SAB. The current can be seen to increase our MOT efficiency until between 2.45 and 2.5 amps, where the MOT pressure increases to the point where efficiency drops and the signal strength greatly decreases.

In this case, it is shown that peak SAB is achieved at approximately 2.47 Amps of current through the rubidium cell, which was set as the operating level for the remainder of the experiments.

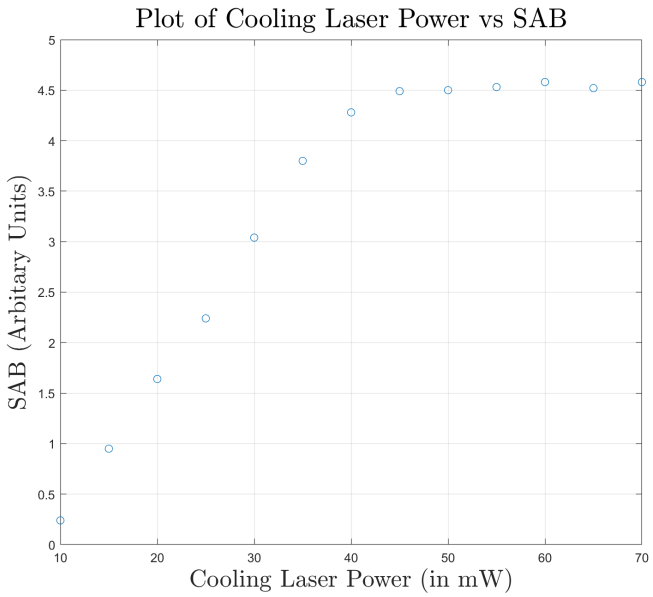

Figure 4.5. Atomic beam fluorescence versus cooling laser power. Plot is used to determine optimal value of laser power without saturation.

Once the correct current was dialed into the MOT, the next step was to determine the optimal power settings on the cooling laser for the new cell. The cooling laser power level was lowered then increased incrementally and again the fluorescence was collected using a scanning detection laser. The resulting fluorescence SAB was recorded. The resulting data is shown in Figure 4.5. The results match up closely with the data taken at the existing cell [19] and the roll off after 45mW cooling power can be observed.

4.2.2 Detection Laser Power Calibration

The aim of this experiment was to determine the optimum detection laser power for the new detection laser assembly / atom beam configuration.

To perform this measurement, the detection laser power was varied by controlling the offset voltage sent to the detection laser acousto-optic modulator (AOM). The AOM is a component (Isomet 1205C-2-804B) in the detection laser and optical pump assemblies that utilizes sound waves to modulate laser frequency, intensity and diffraction. For this experiment it is the intensity modulation property of the detection laser AOM that we are exploiting. By varying the offset voltage sent to the AOM the detection laser power can be modulated from 0 to 9 mW. The corresponding MOT signal above background was recorded at the various output power levels. The results were plotted

in Figure 4.6.

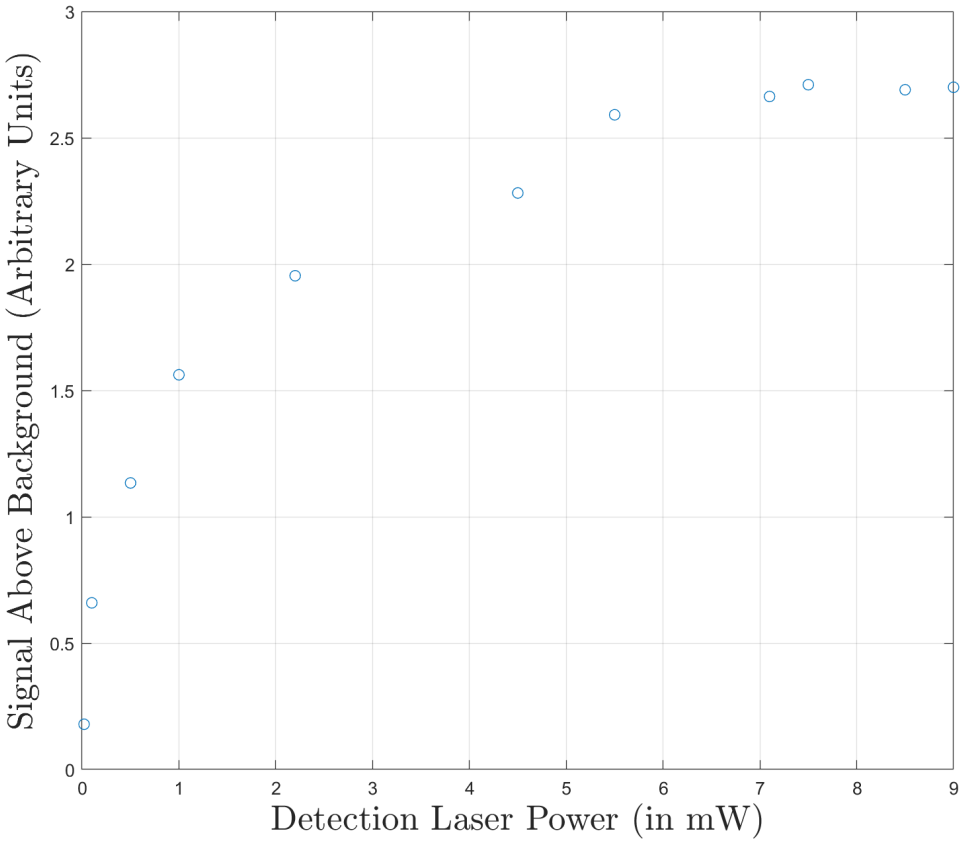

Figure 4.6. Detection laser power versus SAB. The roll off in SAB can be noted after 7mw as the detection laser saturates the chamber.

As expected, SAB rises in concert with detection laser power up to around 7mw of power, at which point the detection laser power saturates the atoms and a roll off in the SAB can be observed. Prior to this experiment the detection laser output was set to a 1 cm transverse sheet beam with a depth of approximately 2mm. This was found to give the optimal results when combined with correct laser power settings to detect all the atoms from the diverging atomic beam without causing unnecessary scattering, and was consistent with values used in the existing detection laser assembly [19].

4.2.3 Beam Divergence

The next step in characterization was to get an indication of the atom beam size and beam divergence within the vacuum chamber. To conduct this experiment, the detection laser assembly was adjusted

to a completely vertical orientation and set up in the chamber closest to the right hand cell aperture. The CCD camera was relocated to face that first right hand side window and was used to get a picture of a "slice" of the beam and saved in .bmp file to preserve information. The detection laser was then adjusted to off resonance, and the picture taken in again in that first position. This second picture was the background level of the laser light within the cell and could be subtracted from the first to get an accurate indication of the beam within the chamber.

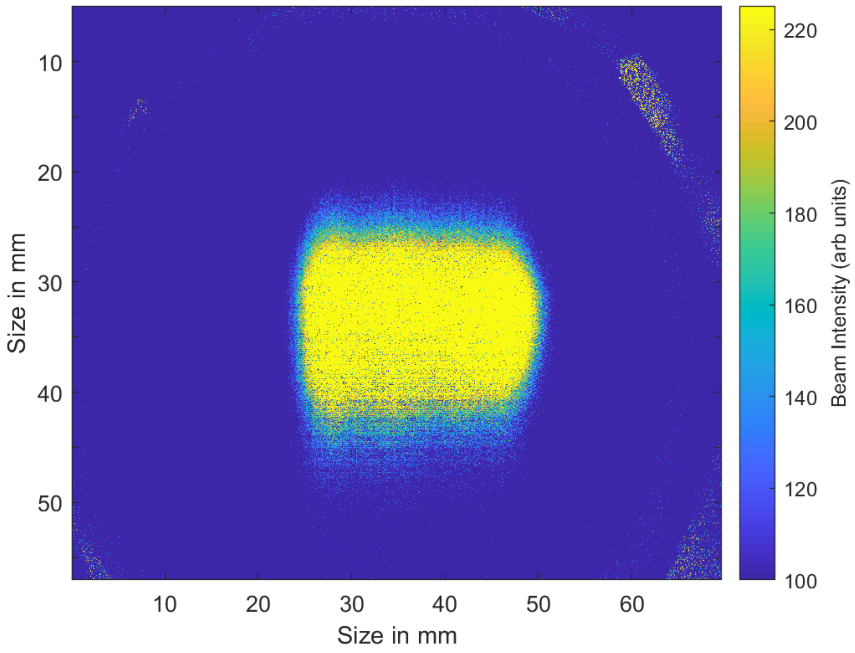

Figure 4.7. Picture of atom beam closer to the aperture (rightmost window).

After the first set of pictures were taken, the detection laser was horizontally translated down the long axis of the chamber to a new position, slightly offset from the first and the process repeated. After 20-30 such pictures, the data was then combined and analyzed in MATLAB to get a clear picture of the beam size in the first chamber

This experiment was then conducted again on the left most window (farthest window from the right cell) in order to get an indication of beam divergence along the long axis of the chamber between windows. Unsurprisingly, the beam at the 3rd window was larger than in the first window and shows the divergence in the beam as it travels along the chamber.

In order to determine the strength of the atom beam vs background hot atoms (caused when hotter/faster atoms escape being cooled in the 2D-MOT and enter the vacuum chamber), a second

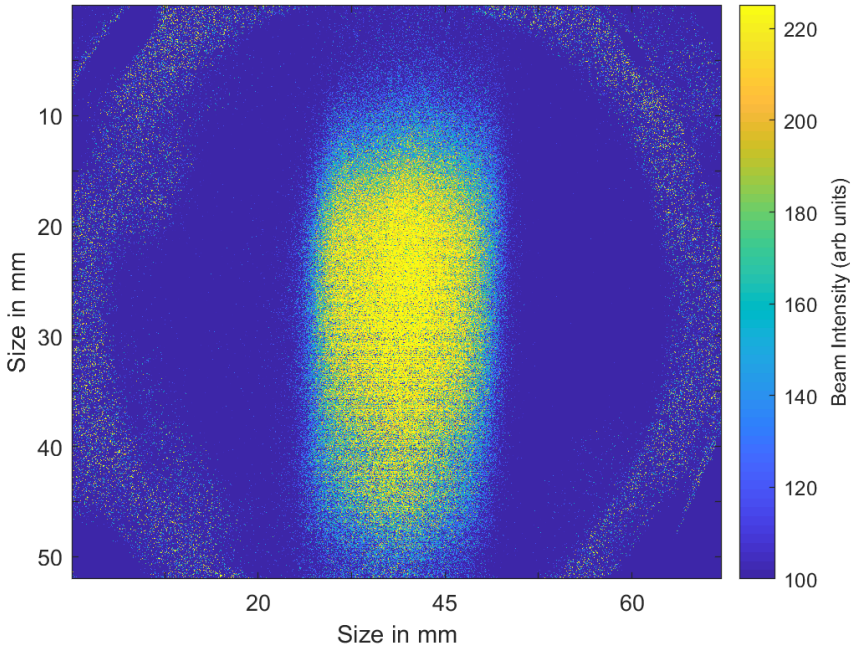

Figure 4.8. Picture of atom beam farther from the aperture (leftmost window).

picture run was then conducted in the 3rd window and partway through the experiment the cooling laser lock was deliberately broken, resulting in a loss of the 2D-MOT and atomic beam. In Figure 4.10, we can see the effect on the picture was soon as the MOT was disrupted, leading to an immediate loss of intensity in the beam and demonstrating that our pictures are indeed of the atom beam and not some other phenomenon.

The next step in determining the beam divergence was using our beam pictures to get a "vertical slice" of the atom beam. Two vertical slices, each from the center of their respective window were then digitized and their respective vertical intensity profiles fit to a Gaussian curve using MATLAB. In this fashion, we were able to find the full width half maximum (FWHM) from each of the center window positions using the method below.

We fit the data to a Gaussian function of the form:

$$f(x) = \frac{A}{\sigma\sqrt{2\pi}} \exp\left[-\frac{(x-b)^2}{2\sigma^2}\right] \tag{4.1}$$

where σ is the standard deviation.

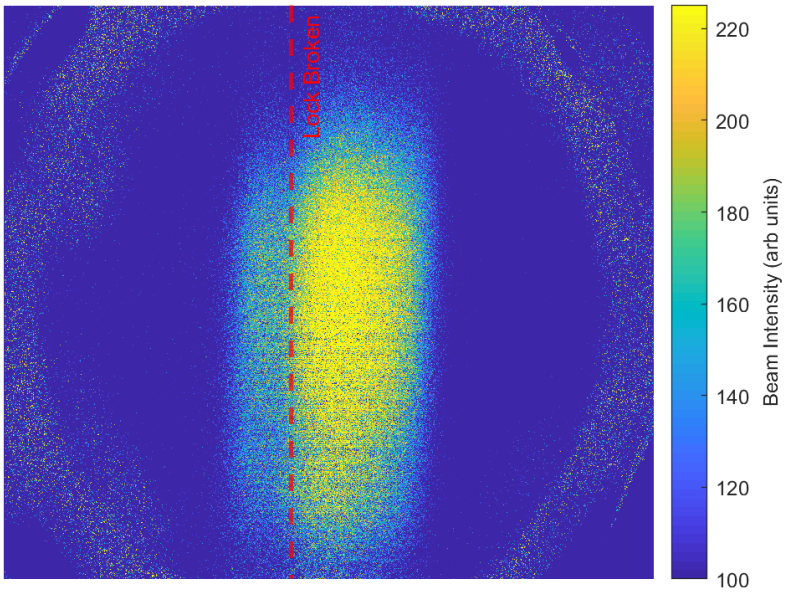

Figure 4.9. Picture of atom beam in leftmost window. Position of break in lock indicated. The detection laser was swept right to left, therefore, pictures taken after the break in lock are to the left of the dotted red line.

The constant scaling factor A can be ignored, resulting in the following equation to solve for the FWHM

$$\frac{1}{2}f(x_{max}) = \exp\left[-\frac{(x-b)^2}{2\sigma^2}\right] \tag{4.2}$$

which when solved yields

$$FWHM = 2\sqrt{2ln2}\sigma \tag{4.3}$$

or

$$FWHM = 2.3548\sigma \tag{4.4}$$

Using this FWHM value, as well as the known distance between the two positions, we can then

calculate the divergence of our atomic beam using Equation 4.5, where $\mathcal{L}$ is the distance between the two windows. Using the tabulated fit data in table 4.1, we found a divergence of 60.5 *mrad*. The result shows a higher divergence when compared to the result of 56 *mrad* measured on the existing left side beam [19].

$$Divergence_{(mrad)} = 2\arctan\left(\frac{FWHM_1 - FWHM_2}{2\mathcal{L}}\right) \tag{4.5}$$

Although the difference in divergence between left and right atom beams are close, the expected result of the newer beam was that our divergence would be smaller due to the faster atom velocity (Section 4.2.4), not larger. The cause of the larger divergence of the atom beam is still under investigation, as there may be differences within the cells as well that could be factors in the larger divergence.

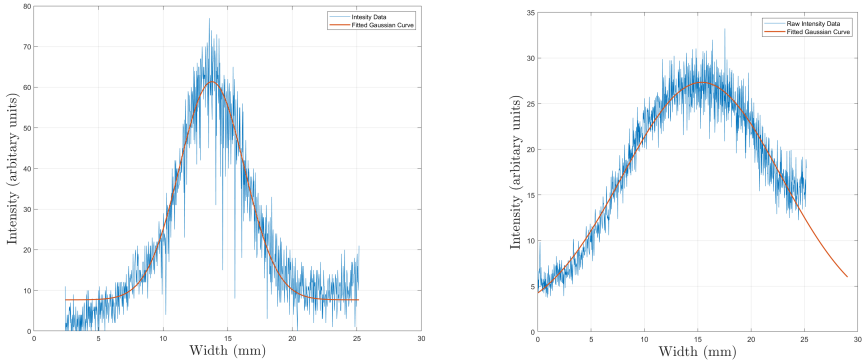

(a) The right Side window (b) The left side window

Figure 4.10. Gaussian fit of the atomic beam intensity, as taken from the center point of both the right and left windows in the vacuum chamber. Due to the divergence of the beam in the left window and the geometry of the CCD camera, the entire curve was unable to be captured.

$$\mathbf{a}\exp\left[-\frac{(x-\mathbf{b})^2}{2\boldsymbol{\sigma}^2} + \mathbf{d}\right] \tag{4.6}$$

Fit Constant	a	b	σ	d
Close Window	53.67	13.78	2.51	7.68
Far Window	26.23	15.37	7.465	1.1

Table 4.1. Fit data from Gaussian fit of atomic beam intensities, used to calculate FWHM as well as beam divergence

4.2.4 Velocity Measurement

The aim of this experiment was to determine the most probable velocity of the atoms in our atomic beam. The first step was to re-configure the optical pump laser solely for this experiment to run longitudinally down the long axis of the vacuum chamber. In this configuration, the laser beam enters through the far MOT cell, passing down the long axis of the vacuum chamber (anti-parallel to the newly created atomic beam) and finally through the far cell where it exits the apparatus.

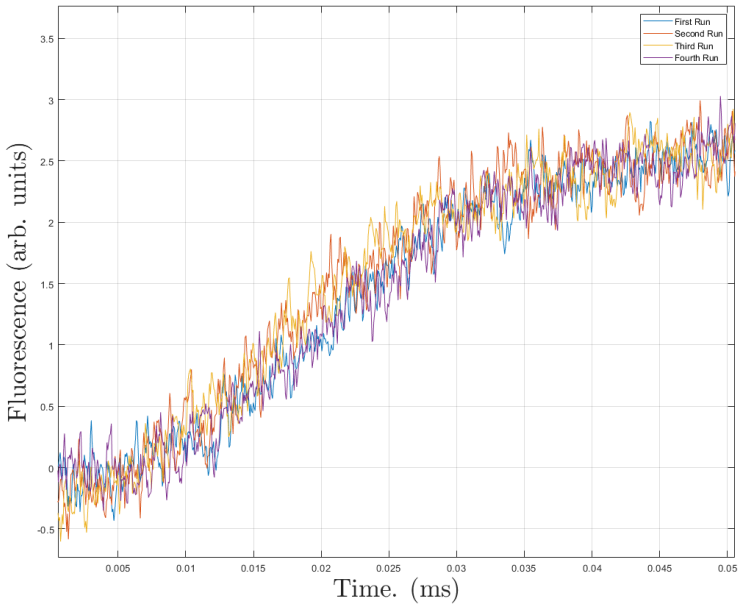

Figure 4.11. The four data runs plotted on the same graph, results were consistent across all runs.

In normal operation the AOM of the optical pumping laser is configured to send a mix of the zeroth and first order—that is to say, frequency shifted—light to the rubidium cell. This was experimentally found to provide the correct mix of light for optical pumping [19]. For this experiment, the AOM of the optical pump laser was adjusted so that *only* the zeroth order passed to the fiber entering

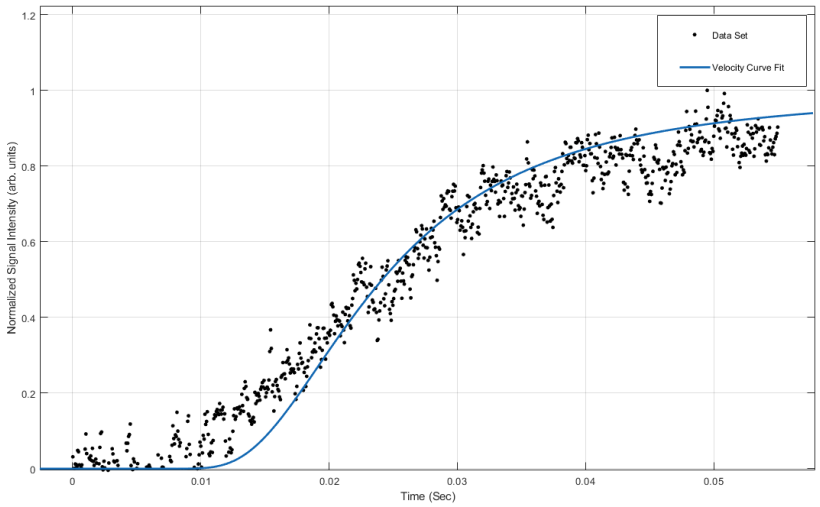

Figure 4.12. Fluorescence data captured during the velocity trial run, shown against the curve fit of Equation 4.7, with N = 1, L = 26 cm, and V_p = 9.0 m/s
.

the cell—in this configuration, the optical pump acts similar to the cooling laser in that it "blocks" the atom beam from entering the vacuum chamber, in effect acting as a plug to the atomic beam. Controlling the AOM with a function generator, the atom beam can be switched 'on' and 'off' at specific times by turning the AOM on and off, allowing for precise timing control of the atom beam. With the detection laser locked on resonance, we then block the atom beam for some time before abruptly switching the laser beam "off", and observing after some time the rise in fluorescence, then switching the beam "on" and observing the fall off as the atoms are blocked. The rise in fluorescence can then be measured against the following approximated formula:

$$\tilde{S} = \frac{N}{V_p^2}\left[e^{-(a^2/V_p^2)}\left(a^2 + V_p^2\right)\right] \tag{4.7}$$

where S is the normalized signal intensity, N = 1, (mapped to our florescence), a is $\frac{L}{t}$ where L is the length traveled by the atoms to the detection beam and t is our time in seconds, and V_p is the velocity of interest, also known as the most probable velocity. This formula assumes that that $L >> \ell$ where ℓ is the cell length. For a full derivation of the above formula including the version without the approximation see Appendix C.

In Figure 4.12, we can see that we have a fit to a V_p of 9.0 m/s. This represents an increase over

similar measurements with the existing atomic beam [19]. This slight increase in velocity was not unexpected, as the MOT laser beam is longer it allowed for faster atoms to be captured within the MOT. The higher velocity is at odds with the larger divergence seen in Section 2.2.3, and the cause of this slight discrepancy is still under investigation.

THIS PAGE INTENTIONALLY LEFT BLANK

CHAPTER 5:
Conclusion and the Way Ahead

Building on the foundation of the existing apparatus, I have constructed a second 2D-MOT laser optics cage assembly as well as doubled the detection and optical pumping assemblies to allow for dual beam operation of the interferometer apparatus. The new cage assembly includes a number of design changes that improve the optical characteristics of the second 2D-MOT as well as bringing user improvements in the form of more convenient power output measurement.

Using the new beam, I conducted experiments to determine the optimal cooling and re-pump laser power settings, as well as the adjusting the current through the rubidium cell to produce the strongest MOT fluorescence. Experimenting with the newly formed second atomic beam, I then characterized the beam itself, measuring beam width and divergence, as well as atom velocity and finally determining optimal detection laser power settings. With the exception of the beam divergence discrepancy, all of these experiments yielded good data, consistent with both theory and prior data taken on the existing cage assembly. This work takes a large step towards turning the apparatus from an interferometer into a proper atomic gyroscope, capable of measuring rotation and acceleration and forming the basis for the next generation of INS.

Work remains to complete the dual beam operation of the system. While the system is set up for dual beam operation, procurement issues and time constraints resulted in an inability to install the second PMT assembly. This installation is necessary before experiments with simultaneous dual beam measurement can take place. Moving forward, after the installation of the second PMT, the next step would be static dual beam experiments. This would allow for the comparison of the output of both beams, which would be vital before moving on to more complicated experiments involving Raman laser interference.

Furthermore, since this apparatus uses continuous beams which are also not spatially separated, work will need to be done to verify our simultaneous measurements. Specifically, as we have not yet conducted simultaneous measurements from both beams, we will need to prove that the optical pump and detection beam set up effectively blocks any interference between beams before continuing on to experiments involving a measurement Earth's rotation, followed by trials using the sum and difference between both beams to measure acceleration and rotation of the apparatus itself. In order to conduct experiments that measure the Earth's rotation, there may need to be a possible re-alignment of the apparatus itself, by aligning the sensing axis of the gyroscope to the

rotation axis of the Earth.

The long-term impact of this bold new technology has yet to be realized, however, I remain extremely excited for the future of this project. Once hardened and miniaturized, this apparatus could form the basis for a new type of super-accurate and stable INS that would revolutionize navigation in traditional GPS denied environments, such as in submarines or conflict zones throughout the globe. Once adopted, this could result in a huge improvement in dived navigation for submarines around the world. The ability to know where you are underwater is often requires challenging contour navigation or risking exposure to enemy aircraft or ships in raising a mast to get a GPS fix, or relying on a very large pool of uncertainty with traditional gyros. The ability to have a highly accurate atomic beam gyroscope based INS would massively increase the amount a time a submarine could stay safely deeply submerged and yet still have an accurate navigable position to from which to work. This benefit is doubly important in contested littoral zones, where tight waters and narrow passages highlight the limits of current RLG based INS used by submarines throughout the globe.

APPENDIX A:
Calculation of Branching Rates for the Optical Pumping Laser

In order to ensure the atoms are in the proper state F = 2 to perform experiments in the vacuum chamber we used a laser as an optical pump. This laser was tuned to F = 3 to F' = 2 transition, where from the F' = 2 state they will decay into F = 2 and F = 3, with four times more atoms ending up in the F = 2 state due to the following branching ratio calculations:

			Excited States ($5^2P_{3/2}$)												
			F' = 2					F' = 3							
		m_F	-2	-1	0	1	2	-3	-2	-1	0	1	2	3	
		-2	7/27	7/54				2/9	2/27	2/135					
		-1	7/54	7/108	7/36				4/27	16/135	2/45				
	F = 2	0		7/36		7/36				4/45	2/15	4/45			
		1			7/36	7/108	7/54				2/45	16/135	4/27		
		2				7/54	7/27					2/135	2/27	2/9	
Ground States ($5^2S_{1/2}$)		-3	5/63					5/24	5/72						
		-2	5/189	10/189				5/72	5/54	25/216					
		-1	1/189	8/189	2/63				25/216	5/216	5/36				
	F = 3	0		1/63	1/21	1/63				5/36		5/36			
		1			2/63	8/189	1/189				5/36	5/216	25/216		
		2				10/189	5/189					25/216	5/54	5/72	
		3					5/63						5/72	5/24	

Figure A.1. Squared transition dipole moments for a portion of the ^{85} Rb D2 transition, in arbitrary units. Source: [19].

In order to calculate the relative branching ratios, we must sum all of the elements in the magnetic sub-levels, which equates to summing the rows.

For F = 3:

$$F' = 2 \text{ to } F = 3 => \frac{5}{63}+\frac{5}{189}+\frac{10}{189}+\frac{1}{189}+\frac{8}{189}+\frac{2}{63}+\frac{1}{63}+\frac{1}{21}+\frac{1}{63}+\frac{2}{63}+\frac{8}{189}+\frac{1}{189}+\frac{10}{189}+\frac{5}{189}+\frac{5}{63} \tag{A.1}$$

which results in a sum of $\frac{35}{63}$.

For F = 2:

$$F' = 2 \text{ to } F = 2 => \frac{7}{27}+\frac{7}{54}+\frac{7}{54}+\frac{7}{108}+\frac{7}{36}+\frac{7}{36}+\frac{7}{36}+\frac{7}{36}+\frac{7}{108}+\frac{7}{54}+\frac{7}{54}+\frac{7}{27} \tag{A.2}$$

which results in a sum of $\frac{35}{18}$.

Taking the ratio between the two

$$\frac{F' = 2- > F = 2}{F' = 2- > F = 3} = (\frac{35}{18})(\frac{63}{35}) = \frac{7}{2} \tag{A.3}$$

Therefore, it is $\frac{7}{2}$ or 3.5 times more likely that an atom in the F' = 2 state will decay into F = 2 than F = 3, which makes this transition perfect for use as an optical pump.

In principle, we could use the cooling laser without any re-pump in order to achieve the same effect (see Section 2.1.3), where we showed that after 1600 transitions, the atoms are left in the F = 2 state. However, this approach results in a significant momentum kick to the atomic beam which can result in the beam being misaligned with the aperture and therefore no atomic beam in the chamber [19].

APPENDIX B: Derivation of Acceleration and Rotation Terms in an Atomic Interferometer

The following is an abbreviated version of derivations for calculating the phase terms when dealing with an accelerating or rotating atomic beam interferometer. Full derivations including Coriolis, centrifugal, gravitational and other effects can be found in [25]. Calculations of terms out to the fourth power is available in [26] .

To begin, we start with the fact that the total phase difference of an atom interferometer can be written as:

$$\Phi = \phi_{prop} + \phi_{lp} + \phi_{split} \tag{B.1}$$

where the ϕ_{lp} is the phase shift cause by interaction of the atoms with the light pulses the upper and lower arms of the atomic interferometer, ϕ_{prop} is the phase difference due to free propagation, and ϕ_{split} is due to a mismatch in travel paths, if the interferometer does not close.

For a closed interferometer that is subject to solely a uniform linear acceleration, one can show that $\phi_{prop} = \phi_{split} = 0$, and the sole term remaining is ϕ_{lp}. It can be shown that:

$$\phi_{lp} = \frac{1}{\hbar}\left[\int_{upper} V_{lp} - \int_{lower} V_{lp}\right] \tag{B.2}$$

where V_{lp} is the potential caused by the laser pulses, which can be re-written as

$$\phi_{lp} = -[\phi_{pos} + \phi_{phase}] \tag{B.3}$$

which can then be written as functions of the path length

$$\phi_{pos} = k_{eff}[z(2T) - z_{upper}(T) - z_{lower}(T) + z(0)] \tag{B.4}$$

$$\phi_{phase} = \phi(2T) - 2\phi(T) - \phi(0) \tag{B.5}$$

Equation B.4 represents the phase acquired during atom laser interaction, and Equation B.5 represents any optical phase changes between pulses. In our experiment, we do not adjust the phase between laser pulses, therefore ϕ_{phase} is set to zero. Then we apply Newtonian mechanics to the Equation B.4 to find the phase difference in terms of ϕ_{pos} only:

$$z(2T) = \frac{\hbar k_{eff}}{m} T + 2aT^2 \tag{B.6a}$$

$$z_{upper}(T) = \frac{\hbar k_{eff}}{m} T + \frac{1}{2} aT^2 \tag{B.6b}$$

$$z_{lower}(T) = \frac{1}{2} aT^2 \tag{B.6c}$$

$$z(0) = 0 \tag{B.6d}$$

Solving for ϕ_{pos} and generalizing to three dimensions the result is:

$$\mathbf{\Phi} = \mathbf{k}_{eff} \cdot \mathbf{a}T^2 \tag{B.7}$$

which is the term for the generalized phased caused solely by acceleration used in section 2.3.

For the derivation of the rotation term in atomic interferometry, we begin by considering a rotating frame $\mathcal{R}'$ and an inertial frame $\mathcal{R}$, with coordinates x', y', z' and x, y, z respectively. The Lagrangian in the inertial frame is then:

$$\mathcal{L}'(r', v') = \frac{1}{2} m(v')^2. \tag{B.8}$$

To transform to the rotating frame, we use

$$\mathbf{v}^{'} = \mathbf{v} + \mathbf{\Omega} \times \mathbf{r} \tag{B.9}$$

Using the in-variance property of the Lagrangian in point transformations, we then can write for the Lagrangian in the the rotating coordinate system

$$\begin{aligned} \mathcal{L}(r, v) &= \mathcal{L}^{'}(r^{'}, v^{'}) \\ &= \frac{1}{2} m (v + \mathbf{\Omega} \times r)^2 \\ &= \frac{1}{2} m v^2 + m \mathbf{\Omega} \cdot (\mathbf{r} \times \mathbf{v}) + \frac{1}{2} m (\mathbf{\Omega} \times \mathbf{r})^2 \end{aligned} \tag{B.10}$$

Given that the momentum (from Lagrangian dynamics) is

$$\mathbf{p} = \frac{\partial \mathcal{L}}{\partial v} = m\mathbf{v} + m\mathbf{\Omega} \times \mathbf{r} \tag{B.11}$$

we then end up with a term for the propagation phase

$$\begin{aligned} \psi_{prop} &= \frac{m}{\hbar} \mathbf{\Omega} \cdot \int_{t_a}^{t_b} dt [r(t) \times v(t)] \\ &= 2 \frac{m}{\hbar} \mathbf{\Omega} \cdot \mathcal{A} \end{aligned} \tag{B.12}$$

where $\mathcal{A}$ is the area vector whose magnitude is the area enclosed by the interferometer, and whose direction is given by the direction of atom propagation crossed with the direction of the momentum kick from the Raman beams. In a purely rotating frame, we recover the term used in Section 2.3.

THIS PAGE INTENTIONALLY LEFT BLANK

APPENDIX C:
Derivation of the Velocity Measurement Function

In this section, we will derive the full equation used to find the most probable velocity of our atomic beam in Section 4.2.3.

We start with the following geometry, where we define L as the total length of the cell plus vacuum chamber that the atom travels until it interacts with the detection beam, and ℓ is the smaller length of the Rb85 cell. The interaction with the detection beam is modeled as a Heaviside step function θ, and then our signal function for a single atom is [27]:

$$S_1(v,t) = \theta(x_0 + vt - L) \tag{C.1}$$

The interaction with the detection laser is modeled as a Heaviside step function, rather than a delta function, to account for the fact that atoms are continuously emanating from the atomic source. Where x_0 is our initial atom position within the cell and v is the velocity.

The measured signal $\tilde{S}(t)$, is the single atom signal averaged possible values x_0 and v, and is given by

$$\tilde{S}(t) = \int dx_0 \int dv \theta(x_0 + vt - L) P(x_0) P(v) \tag{C.2}$$

where the probability functions are:

$$P(x_0) = \frac{N}{\ell} \tag{C.3}$$

where N is the number of atoms in the 2D-Mot, and,

$$P(v) = \frac{2v^3 e^{-v^2/V_p}}{V_p^4} \tag{C.4}$$

C.2 can be written another way:

$$\tilde{S}(t) =<< S_1 >_{x_0}>_v \tag{C.5}$$

$$\begin{aligned} << S_1 >_{x_0} &= \int \theta(x_0 + vt - L)P(x_0)dx_0 \\ &= \frac{N}{\ell}\int_0^{\ell} \theta(x_0 + vt - L)dx_0 \end{aligned} \tag{C.6}$$

When solving for the above integral we end up with:

$$= \theta(\ell)[(L-vt)\theta(vt-L)+\ell-L+vt]\theta(\ell-L+vt)+\theta(-\ell)[(\ell-L+vt)\theta(vt-L+\ell)+L-vt]\theta(vt-L) \tag{C.7}$$

Since $\theta(\ell) = 1$ and $\theta(-\ell) = 0$ due to the properties of the Heaviside function, we can further reduce the integral to:

$$\begin{aligned} < S_1 >_{x_0} &= [(L - vt)\theta(vt - L) + (vt - (L - \ell)]\theta(vt - (L - \ell) \\ &= -(vt - L)\theta(vt - L) + (vt - (L - \ell))\theta(vt - (L - \ell)). \end{aligned} \tag{C.8}$$

This result allows the velocity integral to be divided into three regimes,

$$< S_1 >_{x_0}= \frac{N}{\ell}\begin{cases} 0 & \text{for} \quad v < \frac{L-\ell}{t} \\ vt - (L - \ell) & \text{for} \quad \frac{L-\ell}{t} < v < L/t \\ \ell & \text{for} \quad v > L/t. \end{cases} \tag{C.9}$$

The integral over the first regime can be discounted as its always zero, the second regime can be calculated as follows:

$$
\begin{aligned}
S_{middle} &= \frac{N}{\ell}\int_{L-\ell/t}^{L/t} vtP(v)dv - \frac{N}{\ell}(L-\ell)\int_{L-\ell/t}^{L/t} P(v)dv \\
&= \left[\frac{Nt}{\ell}\frac{2}{V_p^4}\int_{L-\ell/t}^{L/t} v^4 e^{-v^2/V_p^2}dv\right] - \left[\frac{N(L-\ell)}{\ell}\frac{2}{V_p^4}\int_{L-\ell/t}^{L/t} v^3 e^{-v^2/V_p^2}dv\right] \\
&= [I_1] - [I_2]
\end{aligned}
\tag{C.10}
$$

Solving the above integrals for I_1

$$
\begin{aligned}
I_1 = \frac{2Nt}{\frac{4}{p}}\frac{1}{8}V_p^2[&e^{-a^2/V_p^2}(4a^3 + 6aV_p^2) \\
&- 3\sqrt{\pi}V_p^3\,\mathrm{erf}(a/V_p) - 2be^{-b^2/V_p^2}(2b^2 + 3V_p^2) \\
&+ 3\sqrt{\pi}V_p^3\,\mathrm{erf}(b/V_p),
\end{aligned}
\tag{C.11}
$$

where a and b are the limits of integration, $(L-\ell)/t$ and (L/t), respectively, and erf(x) is the error function.

We also have for I_2,

$$
I_2 = \frac{2N(L-\ell)}{\ell V_p^4}\frac{1}{2}V_p^2\left[e^{-a^2/V_p^2}(a^2 + V_p^2) - e^{-b^2/V_p^2}(b^2 + V_p^2)\right] \tag{C.12}
$$

We can see that these equations are long and quite unwieldy; however, by making an approximation that $L >> \ell$, the middle regime terms go to zero because limits of integration become equal to each other, and the only regime we have to concern ourselves with is the third, where:

$$
<< S_1 >_{x_0}>_v = \frac{N}{\ell}\int_{L/t}^{\infty} \ell P(v)dv. \tag{C.13}
$$

when we substitute the probability function X.4 we obtain the following:

$$
\tilde{S}(t) = \frac{2N}{V_p^4}\int_{L/t}^{\infty} v^3 e^{-v^2/V_p^2}dv \tag{C.14}
$$

Solving the integral:

$$\begin{aligned}\tilde{S}(t) &= \frac{2N}{V_p^4}\frac{1}{2}V_p^2 e^{-v^2/V_p^2}((L/t)^2 + V_p^2) \\ &= \frac{N}{V_p^2}e^{-(\frac{L}{t})^2/V_p^2}\left[\left(\frac{L}{t}\right)^2 + V_p^2\right],\end{aligned} \tag{C.15}$$

where the result, Equation C.15, is used in Section 4.2.3 to fit our fluorescence data.

Figure C.1 shows how close the exact and approximate solutions are, using arbitrary values of $L = 30$ cm, $\ell = 5$ cm, and $V_p = 10$ m/s

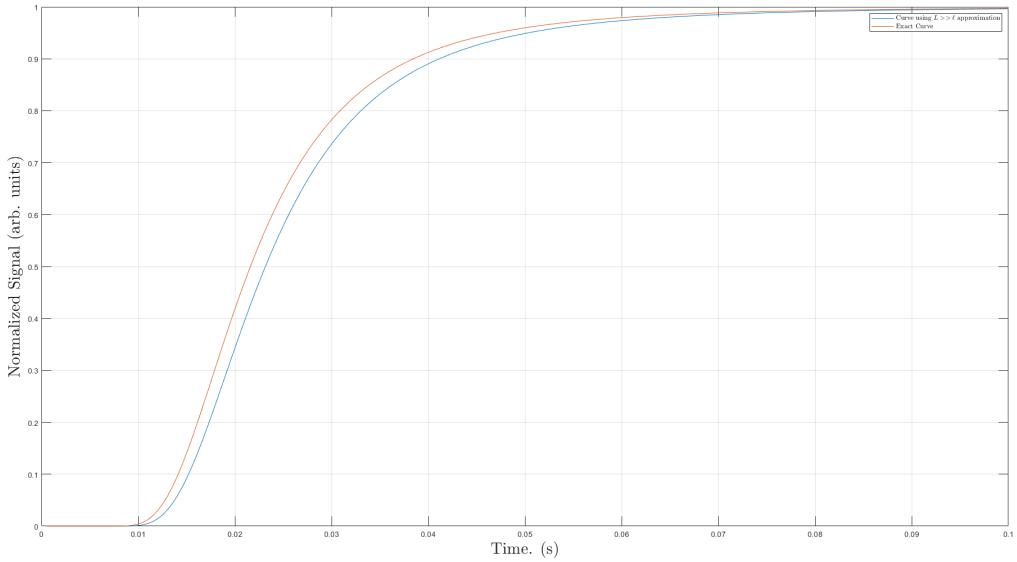

Figure C.1. The exact and the $L >> \ell$ approximation curves for $\tilde{s}(t)$. Input values are arbitrary, chosen only to show closeness of approximation.

List of References

[1] *Global Positing System standard positioning service performance standard*, 5th ed., Washington, DC, 2020.

[2] GPS.gov. (2020). Other global navigation satellite systems. [Online]. Available: https://www.gps.gov/systems/gnss/

[3] G. Leopold. (2016, Feb. 16). Russia is widening the gap in EW. Defense Systems. [Online]. Available: https://defensesystems.com/articles/2016/02/12/russia-ew-capabilities-widening.aspx

[4] V. Passaro, A. Cuccovillo, L. Vaiani, M. Carlo, and C. Campanella. (2017). Gyroscope technology and applications: A review in the industrial perspective. *Sensors (Basel, Switzerland)*. [Online]. *17*(19). Available: https://doi.org/10.3390/s17102284

[5] O. Woodman, "An introduction to inertial navigation," 2007. Available: https://www.cl.cam.ac.uk//techreports/UCAM-CL-TR-696.pdf

[6] Wikipedia contributors, "Sagnac effect — Wikipedia, the free encyclopedia," 2021, [Online; accessed 22-July-2021]. Available: https://en.wikipedia.org/w/index.php?title=Sagnac_effect&oldid=1031246460

[7] M. B. May. (2014, Summer). Ring laser gyro inertial navigation: Lifestyle of a robust technology, Part III. *Institute of Navigation Newsletter*. [Online]. *24*(2). pp. 12–14. Available: https://www.ion.org/newsletter/upload/v24n2.pdf

[8] F. Napolitano. (2010, October). Fiber-optic gyroscopes key technological advantages. *IXSEA Newsletter*. [Online]. Available: https://www.ixblue.com/m/publication/fog-key-advantages.pdf

[9] D. Keith, C. Ekstrom, Q. Turchette, and D. Pritchard. (1991, May). An interferometer for atoms. *Phys. Rev. Lett.* [Online]. pp. 2693–2696. Available: https://link.aps.org/doi/10.1103/PhysRevLett.66.2693

[10] F. Riehle, T. Kisters, J. Helmcke, and C. Bordé. (1991, July). Optical Ramsey spectroscopy in a rotating frame: Sagnac effect in a matter-wave interferometer. *Phys. Rev. Lett.* [Online]. pp. 177–180. Available: https://link.aps.org/doi/10.1103/PhysRevLett.67.177

[11] O. Carnal and J. Mlynek. (1991, May). Young's double-slit experiment with atoms: A simple atom interferometer. *Phys. Rev. Lett.* [Online]. pp. 2689–2692. Available: https://link.aps.org/doi/10.1103/PhysRevLett.66.2689

[12] M. Kasevich and S. Chu. (1991, July). Atomic interferometry using stimulated Raman transitions. *Phys. Rev. Lett.* [Online]. pp. 181–184. Available: https://link.aps.org/doi/10.1103/PhysRevLett.67.181

[13] M. Cadoret, E. de Mirandes, P. Cladé, S. Guellati-Khélifa, C. Schwob, F. Nez, L. Julien, and F. Biraben. (2008, Dec). Combination of Bloch oscillations with a Ramsey-Bordé interferometer: New determination of the fine structure constant. *Phys. Rev. Lett.* [Online]. p. 230801. Available: https://link.aps.org/doi/10.1103/PhysRevLett.101.230801

[14] J. M. McGuirk, G. T. Foster, J. B. Fixler, M. J. Snadden, and M. A. Kasevich. (2002, Feb). Sensitive absolute-gravity gradiometry using atom interferometry. *Phys. Rev. A*. [Online]. p. 033608. Available: https://link.aps.org/doi/10.1103/PhysRevA.65.033608

[15] B. Canuel, F. Leduc, D. Holleville, A. Gauguet, J. Fils, A. Virdis, A. Clairon, N. Dimarcq, C. J. Bordé, A. Landragin, and P.Bouyer. (2006, Jul). Six-axis inertial sensor using cold-atom interferometry. *Phys. Rev. Lett.* [Online]. p. 010402. Available: https://link.aps.org/doi/10.1103/PhysRevLett.97.010402

[16] D. S. Durfee, Y. K. Shaham, and M. A. Kasevich. (2006, Dec). Long-term stability of an area reversible atom-interferometer Sagnac gyroscope. *Phys. Rev. Lett.* [Online]. p. 240801. Available: https://link.aps.org/doi/10.1103/PhysRevLett.97.240801

[17] S. Wu, E. Su, and M. Prentiss. (2007, Oct). Demonstration of an area-enclosing guided-atom interferometer for rotation sensing. *Phys. Rev. Lett.* [Online]. p. 173201. Available: https://link.aps.org/doi/10.1103/PhysRevLett.99.173201

[18] S. M. Dickerson, J. M. Hogan, A. Sugarbaker, D. M. S. Johnson, and M. A. Kasevich. (2013, Aug). Multiaxis inertial sensing with long-time point source atom interferometry. *Phys. Rev. Lett.* [Online]. p. 083001. Available: https://link.aps.org/doi/10.1103/PhysRevLett.111.083001

[19] M. Manicchia, "Construction and characterization of a dual atomic beam accelerometer/gyroscope," Ph.D. dissertation, Applied Physics Dept, Naval Postgraduate School, NPS, 2020.

[20] M. Manicchia, J. G. Lee, G. R. Welch, J. Mimih, and F. A. Narducci. (2019). Doppler-free and Doppler-sensitive Ramsey spectroscopy in a continuous beam of cold atoms. *Rochester Conference on Coherence and Quantum Optics (CQO-11)*. [Online]. p. W6A.2. Available: http://www.osapublishing.org/abstract.cfm?URI=CQO-2019-W6A.2

[21] X.H., "A continuous cold atomic beam interferometer," *J. Appl. Phys*, vol. 117, p. 094901, 2015.

[22] W. D. Phillips, "Laser cooling and trapping of neutral atoms," *Proceedings of the International School of Physics «Enrico Fermi»*, vol. CXVIII, pp. 289–343, 1992.

[23] D. A. Steck. (2019, November). Rubidium 85 D line data. [Online]. Available: http://steck.us/alkalidata

[24] T. Gustavson, A. Landragin, and M. Kasevich. (2000, Jun). Rotation sensing with a dual atom interferometer Sagnac gyroscope. *Classical and Quantum Gravity*. [Online]. pp. 2385–2398. Available: https://doi.org/10.1088/0264-9381/17/12/311

[25] B. Dubetsky and M. A. Kasevich. (2006, Aug). Atom interferometer as a selective sensor of rotation or gravity. *Phys. Rev. A*. [Online]. p. 023615. Available: https://link.aps.org/doi/10.1103/PhysRevA.74.023615

[26] K. Bongs, R. Launay, and M. A. Kasevich, "High-order inertial phase shifts for time-domain atom interferometers," *Applied Physics B: Lasers and Optics*, vol. 84, no. 4, pp. 599–602, Sep. 2006.

[27] F. A. Narducii, A. Black, and J. Burke, "Advances towards fieldable atom interferometers," *Advances in Physics X*, Sep 2021.

THIS PAGE INTENTIONALLY LEFT BLANK

Initial Distribution List

1. Defense Technical Information Center
   Ft. Belvoir, Virginia

2. Dudley Knox Library
   Naval Postgraduate School
   Monterey, California